The Mid-depth Circulation of the Subpolar North Atlantic Ocean as Measured by Subsurface Floats

Kara L. Lavender[a,*], W. Brechner Owens[a], and Russ E. Davis[b]

[a] Woods Hole Oceanographic Institution, Woods Hole, MA 02543, USA

[b] Scripps Institution of Oceanography, University of California, San Diego, La Jolla, CA 92093, USA

June 1, 2004

*Corresponding author: Kara L. Lavender
E-mail: klavender@whoi.edu
Phone: 508-289-2686
Fax: 508-457-2163

Submitted to Deep-Sea Research

Abstract

The multi-year mean, mid-depth circulation of the subpolar North Atlantic Ocean was estimated from direct velocity measurements obtained over a 7.5-year period by 211 neutrally-buoyant, profiling, subsurface floats. We present a statistical analysis of these drift velocity data, and describe the features of the circulation from 400–1500 m depth as measured by the floats. The time-lagged auto-covariances of velocity indicate a Lagrangian integral time scale of approximately 10 days at all drift depths and throughout the basin. Space-time averages of velocity and the associated error ellipses were constructed, and this information was used in an objective analysis to produce estimates of the multi-year mean flow. Estimates of eddy kinetic energy were also computed. The mapped flow depicts a basin-scale cyclonic gyre bounded in the south by the North Atlantic Current. The strongest currents are found along the coasts of Greenland and Labrador, where mean speeds exceed 10 cm s^{-1}. Closed cyclonic recirculations appear just offshore of the boundary currents in the Labrador and Irminger Seas and in the Iceland basin, and also southwest of the Reykjanes Ridge. Topographic steering extends upwards to at least 400 m depth above bathymetry that is significantly deeper, and is most apparent in flow along basin boundaries, around the Reykjanes Ridge, and through gaps in the Mid-Atlantic Ridge. In the center of the basin-scale gyre and to the south of the North Atlantic Current flow is characteristically weak with few large-scale circulation features. There is no indication of a strong linkage along the western boundary from the subpolar to subtropical gyre at depths sampled by floats.

Keywords: *North Atlantic, circulation, subsurface floats, covariance, objective analysis*

1 Introduction

The North Atlantic is the best sampled basin in the World Ocean, yet until recently the large-scale, basin-wide circulation could only be inferred by applying the geostrophic method to hydrographic observations. While valuable in describing the broadest features of the gyre circulation, this method is unsatisfactory because of the necessary but often questionable "level of known motion" assumption, and the limited extent of the hydrographic observations that are used to infer a time-mean circulation. To address these inadequacies a widespread deployment of neutrally-buoyant subsurface floats was included as a major component of the World Ocean Circulation Experiment (WOCE) to directly measure the mid-depth flow field.

In the northern North Atlantic Ocean, more than 200 (P-)ALACE and SOLO floats (Davis et al., 2001) were deployed during the WOCE era. Here we present an analysis of mid-depth drift velocity data collected over a 7.5-year period, representing more than 90% of the expected data return from the full fleet. The direct velocity measurements provided by floats have largely confirmed basin-scale circulation patterns inferred from hydrography, however they have also revealed significant differences from the traditional picture of the circulation. These differences include both "missing" features, such as a pipe-like deep western boundary current, and unexpected features such as recirculations of boundary currents throughout the basin. In this analysis we present data from individual float trajectories, which, although not truly Lagrangian, confirm patterns revealed by the robust statistical analysis of the drift velocity data. The multi-year mean, mid-depth circulation of the entire northern North Atlantic basin, estimated using objective analysis techniques, is presented.

2 Subsurface Float Data Set

The data in this study were obtained from 211 neutrally-buoyant, subsurface P-ALACE and SOLO floats. Floats were deployed in the subpolar North Atlantic Ocean between November 1994 and February 1998 (Fig. 1) as a component of both WOCE and the Labrador Sea Deep Convection Experiment (Lab Sea Group, 1998). The large concentration of floats deployed in the western Labrador Sea coincides with the intense study region of the Deep Convection Experiment, while the more broad-scale deployments delineate WOCE transects.

Each float is programmed to drift at a nominal pressure of either 400 db (39 floats), 700 db (123 floats), or 1500 db (49 floats). Floats that drift at 400 db were designed to measure deep convection and thus were deployed in the western Labrador Sea. To dive from the ocean surface to its target pressure a float adjusts its volume (and therefore buoyancy) by pumping fluid between internal and external reservoirs. Each float drifts at depth for a preset time period ranging from 3.5 to 20 days, then ascends to the surface where it remains for 24 hours to communicate with System Argos satellites. From surfacing and diving positions derived from Argos position fixes, an estimate of the average subsurface velocity is attained.

This study includes all data collected through July 2002, consisting of 21,894 subsurface displacements, or equivalently 578 float years (cumulative) of measurements. Certain data were excluded from the statistical analysis, including displacements from floats that became excessively buoyant (e.g. after losing the wave-damping stability disk) and were unable to submerge (4.7% of displacements), and displacements when floats apparently made contact with the ocean floor (3%). Displacements longer than 40 days, from floats that failed to surface after more than four submergence cycles, were also excluded from the study ($< 1\%$). Errors in estimating surface positions are of the order 3 km (Davis et al., 1992), resulting in subsurface velocity errors of at most 1 cm/s, depending on the length of the submergence period. More than 70% of velocity data were obtained in the three-year period from 1997–1999 when the majority of floats were operational.

Most floats stop reporting after their battery power has been depleted, which occurs after approximately 100 cycles (or 2–5 years) on average. As of July 2002, 20 floats were still reporting data.

In the 7.5-year period of this study floats sampled the entire subpolar gyre of the North Atlantic Ocean, with coverage as far south as 25°N (Fig. 2). Because of the concentrated float deployments in the Labrador Sea the majority of measurements were obtained west of the Mid-Atlantic Ridge. However, the entire subpolar basin is well-sampled north of 44°N. To illustrate the nature of the data, as well as particular flow features, we present maps of selected float trajectories. Although floats are not truly Lagrangian (due to surfacing and the inability to follow vertical motion), these trajectories are indicative of water mass pathways. For example, the trajectories of the six floats in Figure 3 indicate closed or nearly closed cyclonic pathways around the basin. Despite the large ratio of eddy variability to mean velocity, and the inability of floats to track true Lagrangian pathways, these float trajectories depict the large-scale mean flow of the subpolar gyre. Travel time around the basin ranged from 4.0 to 5.7 years and was not correlated with drift depth.

The trajectories of 33 floats drifting at 1500-m depth that visited the Labrador Sea are depicted in Figure 4. Only the portion of each trajectory after the float first entered the basin (either by launch or by drift) is shown. For this purpose the Labrador Sea was defined as west of 43°W and north of 48°N. These 1500-m deep floats sample Labrador Sea Water (LSW), the convectively-formed water mass whose cold, fresh signature has been traced from the Labrador Sea eastward into the subpolar gyre, and also south along the western boundary to subtropical latitudes (Talley and McCartney, 1982; Molinari et al., 1998), presumably having been advected in the deep western boundary current (DWBC). While 18 floats (10 originating in the central Labrador Sea) drifted in the southeastward flow along the Labrador slope, none of these floats travelled south in the DWBC beyond 44°N, just south of Flemish Cap. (The farthest south a float at any depth travelled along the western boundary was 42°N.) Seven floats stopped reporting while in the boundary

current, and two turned offshore near a topographic feature at 50.5°N, 46.5°W (Orphan Knoll). The remaining nine floats reached Flemish Cap before leaving the boundary current. While some floats near Flemish Cap measured strong flow ($O(20\text{ cm s}^{-1})$) along the western boundary at 1500 m depth, others measured equally strong cross-isobath flow. Surface velocities, measured between subsurface drift cycles, depict onshore flow toward the boundary as well as offshore flow in the surface-intensified North Atlantic Current. Therefore, surface drift cannot solely explain the lack of float measurements of the DWBC. Rather, evidence suggests (Lavender et al., 2000; Carr and Rossby, 2001) that near Flemish Cap a vigorous eddy-exchange occurs between the southward flowing LSW and the northward flowing subtropical waters, which could also explain float detrainment from the boundary current.

While eleven of these 1500-m deep floats never left the Labrador Sea, others depicted two main pathways out of the basin. Floats that approached Flemish Cap in the boundary current either drifted offshore to the east or southeast in the eddy-rich flow, or they turned north and exited the basin between 50–53.5°N in the eastward North Atlantic Current. (Note that floats that approached Flemish Cap from the basin interior retroflected to the northwest to remain in the Labrador Sea.) Nine floats drifted eastward south of the tip of Greenland (56–58°N), where all but one entered the Irminger Sea. Four floats eventually re-entered the Labrador Sea from the Irminger Sea, illustrating the close communication between the two basins. Finally, ten of the deep floats that drifted within the Labrador Sea eventually reached the axis of the Mid-Atlantic Ridge, where most then drifted through various fracture zones into the eastern North Atlantic.

Although float lifetimes are finite, the average time a float spent in the Labrador Sea before leaving or failing was computed for each of the 27 floats at 1500-m depth that lived longer than 200 days. Those that eventually left the Labrador Sea did so after an average of 561 days (1.5 years), while those that stopped reporting while in the Labrador Sea had drifted there for an average of 644 days (1.8 years).

The only floats at any depth to exit the subpolar gyre were those that entered the Norwegian Sea either through the Faroe-Shetland Channel or through a gap in the Iceland-Faroe Rise along the northwest edge of Faroe Shelf (Fig. 5). The six floats that entered the Norwegian Sea drifted at depths of 5–1160 m, usually drifting shallower than target depths. Floats drifting along the shelves of the Faroe-Shetland Channel or along Faroe Shelf apparently made contact with the ocean bottom. However, when in the center of the channel three floats drifted freely at depths of 300–600 m. Upon crossing the sill, all floats were funneled northeastward in a narrow current along the eastern boundary of the Norwegian Sea. This flow from the subpolar gyre into the Norwegian Sea was not observed by acoustically-tracked floats drifting at a similar depth in the study by Bower et al. (2002).

Four of six floats that entered the Norwegian Sea originated from west of the Mid-Atlantic Ridge. Although float pathways are not strictly Lagrangian, this supports the idea that advection of warm North Atlantic Current water supplies the Norwegian Sea (McCartney and Mauritzen, 2001). In addition, four floats that were deployed near the eastern boundary south of Rockall Trough (within 80–675 km of the 500 m isobath and between 48.8–51.5°N; not shown) all exhibited net southward movement, providing no evidence for a narrow eastern boundary current supplying Mediterranean Sea water to the Norwegian Sea (Pingree and Le Cann, 1990).

3 Statistical Analysis

The unprecedented basin-wide coverage achieved by these floats permits a robust statistical description of the two-dimensional circulation in the subpolar North Atlantic Ocean. Each float displacement was treated as a point measurement of the average horizontal velocity over the submergence period. From these measurements Eulerian space-time average velocities and their statistical uncertainties were computed. These averages and sampling errors were then mapped using objective analysis techniques to estimate the multi-year mean circulation of the basin and its uncertainty.

3.1 Space-time averages and uncertainties

Let $\mathbf{x}(t|n)$ be the position at time t of the float with label n. The subsurface velocity of the float over the submergence time, τ_n, is defined as:

$$\mathbf{u}(t_n|n) = \frac{1}{\tau_n}[\mathbf{x}(t_n + \frac{\tau_n}{2}\,|\,n) - \mathbf{x}(t_n - \frac{\tau_n}{2}\,|\,n)], \tag{1}$$

where the position of the velocity estimate is assigned to the midpoint of the subsurface displacement. Each velocity estimate was assigned to the nearest point on a specified grid for averaging. The space-time average velocity at location $\mathbf{X}$ was defined as in Davis (1998):

$$\mathbf{U}(\mathbf{X}) = \frac{1}{T}\sum_{n=1}^{N}\mathbf{u}(t_n|n)\,\tau_n, \qquad T = \sum_{n=1}^{N}\tau_n, \tag{2}$$

where N is the number of displacements and T is the total record length (in float days) in the average. Each velocity is weighted by τ_n such that displacements are weighted equally. This gives the minimum mean square error in the space-time average velocity when displacements are uncorrelated (Davis, 1998). The position of the space-time average, $\mathbf{X}$, was assigned to the τ_n-weighted average position of the data, which reduces bias errors caused by non-uniform sampling of an area.

Space-time average velocities were computed from the eight years of drift velocity data adjusted to 700 m depth using climatological geostrophic shears. The averages were constructed on a grid roughly 110 km square, chosen to sample mean spatial structures at scales smaller than the length scale used in the objective analysis, but larger than the assumed scale of eddy variability. Each velocity measurement was assigned to the nearest point on the grid, where the "effective distance" between an observation and a grid point was defined as in Davis (1998):

$$D_{eff}^2 = [(x_g - x_d)^2 + (y_g - y_d)^2] + \left[3\lambda\left(\frac{H_g - H_d}{H_g + H_d}\right)\right]^2 \tag{3}$$

where (x_g, y_g) and (x_d, y_d) are the position of the grid point and datum, respectively. H_g and H_d are the water depth at those positions, estimated from ETOPO-5 bathymetry. When the water depth between a grid point and datum doubles, D_{eff}^2 is increased by λ^2. This attempts to model correlations that are aligned with

bathymetry, as in boundary currents, by effectively elongating the averaging region along isobaths in regions of large topographic gradients. Therefore, the contribution to the average of data spanning these large gradients is reduced. In this analysis $\lambda = 100$ km, which minimizes the across-bathymetry correlations in regions where currents are clearly influenced by topographic gradients (e.g. along the coast of Greenland and along the Reykjanes Ridge).

To account for the vertical distribution of drift data, float velocities were adjusted to a common depth using geostrophic shear computed from the HydroBase 2.0 one-degree smoothed annual climatology of temperature and salinity (Lozier et al., 1995; Curry, 2003). Velocity adjustments from the World Ocean Atlas 1994 climatology (Levitus and Boyer, 1994; Levitus et al., 1994) and the World Ocean Atlas 1998 climatology (Antonov et al., 1998; Boyer et al., 1998) differ from HydroBase 2.0 by more than 2 cm s^{-1}in only 1% of estimates. Most large discrepancies were located either in regions dominated by large eddy variability, or near boundary currents where results of isopycnal and isobaric averaging differ.

The space-time average velocities are presented in Figure 6. The fastest flows are along the northern and western boundaries of the basin and near Flemish Cap, including the subsurface signature of the northward-flowing North Atlantic Current. Flow around the Reykjanes Ridge and the local acceleration through the Charlie Gibbs Fracture Zone illustrate apparent topographic control, while reversing zonal flows exist just north of the Azores Plateau (40–45°N over the Mid-Atlantic Ridge). Flow patterns in the center of the western basin and also in the southeast quadrant of the domain do not depict coherent structures, probably because the record length is too short to resolve weak flow, especially in the presence of high eddy velocity variance. The mean record length per space-time average for much of the basin is less than one year, but increases to almost two years in the Labrador Sea.

The statistical uncertainty (or standard error) of the space-time averages is calculated as the covariance of each average divided by the number of degrees of

freedom in the average, N_{DOF}:

$$\varepsilon_{ij}^2 = \frac{< u_i' u_j' >}{N_{DOF}} = \frac{\sum_{n=1}^{N} (u_i^n - U_i)(u_j^n - U_j)\,\tau_n}{N_{DOF}\ \sum_{n=1}^{N} \tau_n}. \tag{4}$$

Here i, j indicate the velocity component, n is an index of the observations, and N is the total number of observations in an average. The mean velocity, $\mathbf{U}$, was computed using a least-squares fit of nondivergent linear vector functions of position to local space-time averaged velocities on a 100-km scale (Davis, 1998).

To calculate N_{DOF} one must account for the correlation between different floats. Float velocities from points separated by more than the velocity correlation scale all contribute fully to N_{DOF}. In this data set float velocities with time separations of 10 days or less were within 100 km of one another less than 1% of the time. Though the correlation length scale is not well known, it is likely of the order of the Rossby radius for the gravest internal mode, or the Rhines scale, $(U/\beta)^{1/2}$, where U is the rms eddy velocity and β is the derivative of the Coriolis parameter with respect to northward position. The Rossby radius is O(10–20 km) and the Rhines scale is typically less than twice the Rossby radius. This suggests that the correlation length scale is less than 100 km, and the analysis in Section 3.2 confirms this. Therefore, in computing N_{DOF} we neglect the correlation between different floats.

In estimating statistical reliability one must also account for serial correlation of velocity measurements from a single float. The Lagrangian time-lagged autocovariance (Taylor, 1921) is defined as:

$$L_{ij}(\tau) = < u_i'(t|n)\, u_j'(t+\tau|n) > \tag{5}$$

where n is the Lagrangian label, primes indicate departures from the Lagrangian mean for that float, and $< >$ indicates an average over many float records and labeling times t. The time-lagged autocovariances from the three float depths (Fig. 7) show measurements to be essentially uncorrelated (correlations less than 0.25) after 10 days. The integral time scale, obtained by integrating the autocorrelation in Equation 5 from zero to large positive lags, is between 6 and 10 days. This is consistent with previous float observations in the North Atlantic (McWilliams et al., 1983; Böning, 1988).

The number of degrees of freedom for a space-time average was computed as follows. Each time a float moved into a grid cell, the number of degrees of freedom it contributed to the average was computed as the length of time it was in the cell divided by 20 days, a conservative estimate of the double-sided integral time scale. Excursions into a cell of less than 20 days were taken to contribute one degree of freedom. The resulting uncertainties of the space-time averages, computed according to Equation 4, are plotted as error ellipses in Figure 8 for estimates whose mean exceeds its uncertainty. In all but a few averages (all in boundary currents) the rms variability far exceeds the mean. However, across most of the basin the density of observations reduces uncertainties to yield statistically significant sample mean velocities. The uncertainty exceeds the mean in regions such as the interior of the subpolar gyre. Although not statistically different from zero, it is determined that the mean flow in these regions is weak (Fig. 6).

In addition to the uncertainty of the sample mean, errors arise due to the large concentration of floats deployed in the western Labrador Sea. Gradients in float concentration in regions with eddy variability may drive a flux of floats away from the well-sampled region, thereby contaminating the estimate of mean velocity (Davis, 1991). This array bias is estimated as:

$$\mathbf{U}_{array} = -\kappa \cdot \nabla \, ln \, C \tag{6}$$

where κ is a diffusivity and C is the mean float concentration per unit area, smoothed over the time and space averaging intervals. $\mathbf{U}_{array}$ was estimated for the Labrador and Irminger Seas (Fig. 9). The diffusivity was calculated as the covariance about space-time averages ($< u_i' u_j' >$ in Eqn. 4) times a constant integral time scale of 10 days (Freeland et al., 1975). The concentration gradient was estimated from the number of observations in each space-time average using a centered-difference scheme. Because floats cannot drift onto (or from) land, $\mathbf{U}_{array}$ was not computed along the basin boundaries. The estimated bias produces an artificial divergent flow from the deployment region in the western Labrador Sea, and larger values near Flemish Cap where eddy variability is extremely high. Across

the majority of both basins, however, the magnitude of the array bias is smaller than the estimated statistical error.

3.2 Space-lagged Covariances

To assist in defining statistics for the objective analysis, space-lagged covariances were computed for the zonal and meridional velocities adjusted to 700 m depth. For each pair of velocities measured within an integral time scale (10 days) of one another, we computed the zonal (x) and meridional (y) distance between the observations, and their covariance ($< u''u'' >$, $< u''v'' >$, $< v''v'' >$) assuming a zero mean. Covariances were averaged in bins defined by spatial lag in x and y, and over all time. The number of observations in an average ranged from roughly 400 at the largest lags to more than 2600 at the smallest non-zero lag. The spatial correlations (Fig. 10) were normalized by the value at zero lag.

In a two-dimensional (2-D), isotropic, and non-divergent flow, the longitudinal covariance (velocity parallel to the displacement vector) has a longer length scale than the transverse covariance (velocity normal to the displacement vector) (Batchelor, 1953). Consistent with this theory, the longitudinal components of the float velocity covariance ($< u''u'' >$ vs. x-lag at zero y-lag, and $< v''v'' >$ vs. y-lag at zero x-lag) have much longer length scales than the transverse components, while the cross-covariance, $< u''v'' >$, is essentially zero for all lags (Fig. 11). The transverse components ($< u''u'' >$ at zero x-lag and $< v''v'' >$ at zero y-lag) have small or negative lobes at lags larger than 25 km, which is also consistent with 2-D turbulent flow.

Using the geostrophic relationship, these velocity covariances can be expressed in terms of a pressure covariance (Bretherton et al., 1976). The pressure covariance is often assumed to be a Gaussian function of separation with the e-folding scale defining the scale of variability. Here we report scales of variability in terms of the pressure e-folding scale. It is readily apparent that the zero-crossing of the transverse velocity covariance is a fraction (0.707) of the pressure e-folding scale, but that the longitudinal velocity covariance has the same e-folding scale as pressure.

The velocity covariances in Figure 11 indicate two dominant scales of variability. The first has an e-folding scale in pressure of 150 km. Because the transverse and longitudinal covariances for both components of velocity are consistent with this 150 km scale, the covariances are isotropic. The second scale is at 10–20 km (the Rossby radius of deformation), where the covariance is weak but not zero. We associate the larger scale with the spatial structure of the mean flow and the shorter scale with mesoscale variability. The goal of our objective analysis is to map the multi-year mean flow circulation, so we model the "signal" pressure covariance with a 150 km e-folding scale. While the spatial covariances suggest that the flow in the basin has the characteristics of isotropic 2-D turbulence, there are regions where this is not true. The space-time averages depict regions of strong along-isobath flow in the boundary currents and around large topographic features such as the Reykjanes Ridge. Because of topographic steering, these flows are very anisotropic and cannot be described by the statistics of 2-D turbulence.

The statistics of such flows may be partially described by a covariance that includes changes in the barotropic potential vorticity, $\zeta = f/H$, where f is the Coriolis parameter and H is the water depth. We decomposed all float velocities into components parallel ($u''_{\|}$) and normal ($u''_{\perp}$) to the local ζ contour, with H estimated from the Smith and Sandwell (1997) and ETOPO-5 bathymetry databases. Spatial covariances were computed for $u''_{\|}$ and $u''_{\perp}$ between observations within an integral time scale, as above, and averaging bins were defined by the spatial separation and the change in ζ between observations. Essentially no correlation is observed between velocities spanning ζ contours (not shown), or in $< u''_{\perp} u''_{\perp} >$ for observations separated in distance (Fig. 12). However, the $< u''_{\|} u''_{\|} >$ correlation suggests a length scale of roughly 80 km between velocities measured along the same ζ contour. These correlations illustrate the anisotropic nature of the velocity field near strong gradients in barotropic potential vorticity.

3.3 Objective Analysis

The mean mid-depth circulation of the subpolar North Atlantic was estimated using objective analysis techniques. This linear least-squares estimation method (Bretherton et al., 1976) weights each observation according to the statistics of the signal being mapped and the noise in each observation. Because observational sampling errors may be accounted for, this method provides increased accuracy without sacrificing spatial resolution as occurs in space-time averaging. In addition, dynamical constraints may be incorporated into the signal statistics, and the mean square error of the mapped result may be directly estimated.

We adopted the method of Davis (1998) to map the multi-year mean circulation at a particular depth. The signal covariance for pressure was specified, and the signal covariance for velocity was deduced from the pressure covariance using the geostrophic relation:

$$fu = -g\frac{\partial \eta}{\partial y}, \quad -fv = -g\frac{\partial \eta}{\partial x} \tag{7}$$

where $\eta(x,y) = (1/\rho_0\, g)\, p(x,y)$ is the "geostrophic pressure" measured as a height, and f is the Coriolis parameter that varies with latitude. Note that this covariance does not enforce non-divergence of the velocity field.

The geostrophic pressure covariance was assigned the following form:

$$< \eta_i\, \eta_j >= A^2 exp(-R^2), \text{ where} \tag{8}$$

$$R^2 = \frac{(x_i - x_j)^2 + (y_i - y_j)^2}{L^2} + \frac{1}{\Phi^2}\,\frac{(\zeta_i - \zeta_j)^2}{(\zeta_i^2 + \zeta_j^2)}$$

The signal covariance is a function of spatial lag, where (x,y) are the positions of the space-time averages and L is the correlation length scale. The covariance also includes a dependence on the barotropic potential vorticity, ζ, which is weighted by the parameter Φ. This anisotropic form attempts to model the data covariances in Figure 12.

All maps were computed from space-time averaged velocities assuming an *a priori* mean velocity of zero. Note that this *a priori* mean will tend to bias low the

estimates of mapped velocity. Mapping space-time averages rather than drift velocities reduced the size of the matrix to be inverted and therefore its computational cost. In addition, the mean square error computed from the averages (ε_{ij}^2 in Eqn. 4) was included as noise in the model covariance to represent eddy variability at unresolved scales.

In this analysis $L = 150$ km as suggested by the covariances in Figure 11, and A^2 was computed from the mean square space-time averaged velocity. The signal-to-noise ratio was computed as the ratio of A^2 to the mean of the error variances ($\varepsilon_{uu}^2 + \varepsilon_{vv}^2$).

We examined the influence of the barotropic potential vorticity term in the covariance by comparing maps of 700 m flow computed with a strong weighting ($\Phi = 1$) to those with no constraint ($\Phi = \infty$). There were no qualitative differences in the flow patterns between the two maps, and each velocity map was equally well-correlated with the data (Table 1). Where map skill, defined as one minus the ratio of the estimated error variance to the expected signal variance, was greater than 0.7, differences in speed between the two maps were nearly always smaller than the estimated map error. The main differences between maps occurred in flow along basin boundaries. When the potential vorticity term was included, the constrained flow near strong gradients in ζ formed narrower and faster currents that were closer to the boundary (Table 1). Because this result better represents observed boundary currents, all maps presented below were computed with $\Phi = 1$.

4 Objectively Analyzed Mid-depth Circulation

The mean circulation at 700 m depth is presented in Figure 13. This map was computed from float data at drift depths between 200–1800 m that were adjusted to 700 m depth using hydrographic shear estimates. A map computed with float data only near 700 m depth was not significantly different. Map skill is computed in the objective analysis, however it may only be used as a relative measure of uncertainty because of its strong dependence on the details of the *a priori* statistics.

The basin-scale cyclonic subpolar gyre is defined by strong currents along the northern and western boundaries (in the northern Iceland basin, along the Reykjanes Ridge, and in the Irminger and Labrador Seas) and a meandering North Atlantic Current (NAC) to the south that eventually closes the gyre in the east. The locations of named geographic features are shown in Figures 1 and 5. There is no indication of mean southward flow from the subpolar gyre to subtropical latitudes at this depth. The cyclonic flow delineating the subpolar gyre is broadly consistent with Reid's (1994) flow at 800 m inferred from hydrography and tracers, and trajectories of individual floats (Fig. 3) suggest that parcels may follow this mean flow.

The strongest flow in the domain is along the slope of Greenland (East and West Greenland Currents) where speeds exceed 15 cm s^{-1}. The West Greenland Current bifurcates near 61°N into branches that decelerate and follow the 2000 m and 2800 m isobaths around the northern Labrador Sea. This bifurcating flow has been observed as shallow as 15-m depth by surface drifters (Cuny et al., 2002). The two branches rejoin in the western basin to form a southward flow along the slope of Labrador (Labrador Current) where speeds reach 12 cm s^{-1}. There is some indication that the Labrador Current continues south along the boundary beyond Flemish Cap, however the few floats that measured this flow all turned offshore north of 42°N.

Just north of Flemish Cap the northward flowing NAC enters the Labrador Sea and forms the Northwest Corner near 50.5°N, 44°W. The NAC then turns east and accelerates through the Charlie Gibbs Fracture Zone before bifurcating near 53°N, 24.5°W. The southern branch meanders eastward to the entrance of Rockall Trough, however no pressure contours associated with the NAC enter the trough itself. Rather, the flow turns westward and continues around the southern edge of Rockall Plateau into the Iceland basin. The northern branch of the bifurcated NAC meanders into the Iceland basin, where the branches merge to feed the cyclonic boundary flow. The westward flow from the Iceland basin to Irminger basin is

clearly steered by the topography of the Reykjanes Ridge, despite being much shallower than the ridge itself.

Within this basin-scale gyre are a number of sub-basin scale closed cyclonic recirculations not depicted in classical subpolar gyre regimes. The low pressure feature in the northern Iceland basin (61.5°N, 20°W) is closed by a weak recirculation of the boundary flow, while the feature southeast of the Reykjanes Ridge (54°N, 32°W) is bounded by the NAC to the south and east and by flow along the Reykjanes Ridge to the north. These features were observed in trajectories of individual floats, and are qualitatively similar to those measured by acoustically-tracked floats (Bower et al., 2002).

The series of cyclonic recirculations in the Irminger and Labrador Seas were first described by Lavender et al. (2000) from an early subset of these float data. These features are defined by an anticyclonic flow offshore of the cyclonic boundary currents that is clearly visible in Figure 13b. Individual float trajectories illustrate the nature of these low pressure regions. In Figure 14a select float displacements near the tip of Greenland indicate eastward flow into the Irminger Sea. One float entered this flow from the boundary current, two entered from the central Labrador Sea, and one float was deployed into the eastward flow before it turned back and joined the boundary current. Trajectories from all four floats, at depths between 400–1500 m, depict eastward flow that closely follows the 3000 m isobath. This is suggestive of topographic control at depths much shallower than the bathymetry. Other floats in this region have looping trajectories (Fig. 14b) between the boundary and offshore currents, and similar features are observed along the western boundary of the Labrador Sea (Fig. 14c). While such trajectories clearly contribute to the cyclonic recirculations in the mean field, we cannot determine whether individual floats sampled time-dependent eddies or permanent features. Spall and Pickart (2003) suggest the cyclonic recirculations in both basins result from strong wintertime wind forcing in the western Irminger Sea that drives time-dependent, stratified, topographic beta-plume dynamics. They argue that once the seasonal

forcing has abated, baroclinic Rossby waves interact with bottom topography to maintain the recirculations throughout the year.

Flow to the south of the subpolar gyre (i.e. south of the NAC) is extremely weak, with the exception of a series of reversing zonal flows observed northeast of the Azores islands (40–46°N, 19–31°W). The associated high and low pressure centers form a dipole, with speeds in the intermediate westward flow exceeding 5 cm s^{-1}. In addition, there is a meandering northward flow near the eastern boundary of the basin that originates south of Porcupine Bank (52°N, 14°W). This flow splits, with one branch flowing north into the Iceland basin, and the other entering Rockall Trough where an anticyclonic circulation is observed.

We cannot determine from float data alone whether a continuous mean flow exists from the North Atlantic to the Norwegian Sea through Rockall Trough. The mapped field indicates a northward flow within Rockall Trough (Fig. 13), however only two floats followed this path into the Norwegian Sea (Fig. 5). One float was deployed in Rockall Trough, while the other was deployed on the eastern side of the Mid-Atlantic Ridge and drifted for 1.3 years in the NAC before reaching Rockall Plateau. The temperature and salinity at drift depth along this trajectory varied significantly (7.2-12.2°C, 35.0-35.7 psu), with the coldest and freshest water encountered southwest of the entrance to Rockall Trough. It is not clear whether the change in properties is a signature of significant mixing, or of distinct water masses and therefore a result of the non-Lagrangian nature of the float measurements.

4.1 Depth Dependence

To examine variations in the flow with depth we computed maps of mean flow at 400 m from floats drifting between 200–500 m depth, and at 1500 m from floats drifting between 1000–1800 m depth (Fig. 15). At all levels the cyclonic boundary currents defining the subpolar gyre and the low pressure centers within the gyre are present. However, differences do exist. At 400 m the meandering of the NAC is stronger than at deeper levels, perhaps because of weaker topographic control. The NAC does not enter the Iceland basin in the mapped flow at this level. Instead, it

wholly recirculates in the broad low pressure feature southeast of the Reykjanes Ridge, suggesting that flow in the Iceland basin is dominated by two isolated cyclonic gyres. However, because most floats ballasted to 400 db were deployed in the western Labrador Sea, flow in the Iceland basin at this depth was poorly sampled. Some floats did measure a cyclonic boundary current in the Iceland basin, but there were too few observations to reliably map this flow. From the western Iceland basin the flow is steered, even at this shallow depth, by the Reykjanes Ridge into the Irminger basin, where it then merges with northeastward flow from the Labrador Sea. Together these currents feed a cyclonic recirculation that is broader than the recirculations observed at deeper levels.

At 1500 m depth (Fig. 15b) most flow features are similar to but weaker than those at shallower depths. We computed the difference between mapped velocity at 400 m and 1500 m depth, and compared this to the geostrophic velocity at 400 m relative to 1500 m depth estimated from hydrographic data (courtesy of R. Pickart). The hydrographic data consisted of a 10-year average of repeated hydrographic sections along the cross-basin AR7W line in the Labrador Sea (Fig. 16). This hydrographic estimate gives relative velocities of less than 1 cm s^{-1}everywhere but in the strong boundary currents. The estimated velocity difference from mapped float data is larger, but cannot be distinguished from zero at the 95% confidence level. One can only conclude that flow through this transect in the Labrador Sea is weakly depth-dependent everywhere except along the basin boundaries.

4.2 Variability

The single-particle Lagrangian time-lagged autocovariances of float velocities, first introduced in Section 3 to estimate the Lagrangian integral time scale (Fig. 7), illustrate the nature of the velocity variability. As can be inferred from the time-lagged autocovariances and the error ellipses in Figure 8, eddy velocities are remarkably isotropic at all depths. The eddy variance decreases with increasing depth from 400 to 1500 m. Time-lagged autocovariances computed independently for regions east and west of the Mid-Atlantic Ridge revealed slightly higher

variances in the western basin due to the strong boundary currents and the large variability near Flemish Cap.

Eddy kinetic energy (EKE) at 700 m depth (Fig. 17) was estimated from the variance of float drift velocities about local fits of nondivergent linear vector functions of position to the space-time averaged velocities. Use of this filtered mean, as opposed to the objectively-analyzed field, reduced the artificial contribution due to smoothing of the mean to eddy variability. The eddy velocity covariances have been decomposed into principle components (Fofonoff, 1969), however there is no statistically significant anisotropy since the ratio of the major to minor axes never exceeds the F-test criterion at the 95% confidence level (DeGroot, 1989). As a result, we show only a map of EKE.

The highest EKE at 700 m depth in the subpolar gyre region was observed offshore of Flemish Cap. While the center of this maximum is coincident with that observed in surface EKE estimates (White and Heywood, 1995; Fratantoni, 2001), we did not observe similarly elevated EKE along the NAC eastward of 33°W. In addition, EKE magnitude at the maximum near Flemish Cap estimated from acoustically-tracked floats at comparable depths (500-900 m) was roughly three times greater than values reported here (Carr and Rossby, 2001). We attribute this difference to the temporal low-pass filtering inherent in the longer sampling period of profiling versus acoustically-tracked floats. A comparable discrepancy in EKE magnitude was observed by Fratantoni (2001) when comparing EKE computed from satellite altimetry (10-day resolution) to that from surface drifters (6-hourly resolution).

A local maximum in EKE was also observed in the boundary currents around the tip of Greenland, including an offshore extension centered at 60°N, 49°W. This extension nearly coincides with the EKE maximum observed in satellite altimetry (White and Heywood, 1995; Prater 2002) and surface drifter data (Fratantoni, 2001; Cuny et al. 2002), and occurs near the change in topographic slope marked by the offshore divergence of the 3000 m isobath. Bracco and Pedlosky (2003), using an idealized model of quasigeostrophic flow in a two-layer channel, suggest that eddies

may be formed in this region by a locally unstable baroclinic flow interacting with the sloping topography. Eden and Böning (2002), on the other hand, in a study of energetics in a high-resolution model of the Labrador Sea, argue that eddies are spawned by barotropic instability of the West Greenland Current where it encounters a change in topographic slope.

5 Summary and Discussion

Subsurface floats have provided unprecedented basin-wide measurements of velocity in the subpolar North Atlantic Ocean, permitting a robust statistical description of the mid-depth circulation. The circulation of the subpolar gyre is dominated by strong boundary currents, with speeds exceeding 10 cm s^{-1}along the continental slopes of Greenland and Labrador. The cyclonic gyre is closed in the south by the meandering North Atlantic Current (NAC), and the region south of the NAC is generally characterized by weak flow with few large-scale circulation features. There is no indication of a strong linkage along the western boundary from the subpolar to subtropical gyre at depths sampled by floats.

The subpolar gyre depicted by float data is contracted to the west compared to other circulation schemes (e.g. Reid, 1994; Lozier et al., 1995). In the mean field none of the flow originating in the western basin reaches the eastern boundary or enters Rockall Trough. These results suggest that LSW was not advected by the mean flow to the eastern boundary during the sampling period of the floats, although water with LSW properties had been observed in the area 5–10 years earlier (Arhan et al., 1994; Cunningham and Haine, 1995). Bersch et al. (1999) suggest that in the late 1990's a westward shift of the Subarctic Front (or NAC) in the Iceland Basin occurred in response to a weakening of the westerlies, as indicated by a shift in the North Atlantic Oscillation. Such decadal variability could explain a change in LSW pathways, which in turn could affect the meridional heat transport in the North Atlantic Ocean.

Raw velocities and mapped fields clearly illustrate topographic steering, which extends upwards to at least 400 m depth above bathymetric features that are significantly deeper. This is most apparent along the basin boundaries, around the Reykjanes Ridge, and in eastward flow through gaps in the Mid-Atlantic Ridge. This is not surprising since the influence of topography, or of barotropic potential vorticity (f/H), on the drift of acoustically-tracked floats has been documented by previous authors (e.g. Rossby et al., 1983; LaCasce, 2000). That floats drifting as shallow as 400 m depth are influenced by topography hundreds of meters below suggests that barotropic currents may dominate flow in these regions (LaCasce, 2000).

Smaller scale cyclonic gyres are located in the vicinity of boundary currents in the Labrador and Irminger Seas, the Iceland basin, and southwest of the Reykjanes Ridge. In the Labrador and Irminger Seas these recirculating gyres may enhance open-ocean deep convection by trapping water where it may be repeatedly exposed to large wintertime surface heat fluxes (Lavender et al., 2002; Pickart et al., 2003). The large heat losses drive deep convection and the formation of intermediate-depth LSW. Active deep convection has been frequently observed within the region of the recirculation gyre in the western Labrador Sea (Lazier, 1973; Lilly et al., 1999; Pickart et al., 2002), and more recently also in a second region southwest of the tip of Greenland (Lavender et al., 2002). In fact, one float drifting in the cyclonic gyre just southwest of Greenland observed mixed layers gradually deepening to 1100 m depth, indicative of active deep convection (Fig. 18).

From either the western Labrador Sea or the formation region southwest of Greenland, LSW may enter the 2–5 cm s^{-1}anticyclonic flow that directly feeds the Irminger Sea to the east. While LSW formed southwest of Greenland could certainly reach the Irminger Sea in less than six months (Sy et al., 1997), water from the western Labrador Sea could take much longer. Of the few floats that drifted from the western basin to the Irminger Sea, those drifting at 400 m depth arrived in less than 7 months, while deeper floats travelled for 10–18 months. It is clear that the

recirculating gyres and boundary currents closely link the two seas, suggesting that deep convection in one basin may be sensitive to heat loss within the whole region.

Acknowledgements

We thank J. Dufour, J. Sherman, J. Valdes, R. Tavares, and B. Guest for technical development and preparation of the floats, D. Newton, C. Wooding and B. Jones for help with data processing, and the many scientists who deployed the floats at sea. R. Pickart kindly provided hydrographic data along the AR7W line in the Labrador Sea. KL was supported by the Postdoctoral Scholar Program at the Woods Hole Oceanographic Institution, with funding provided by the J. Seward Johnson Fund. This work is supported by the Office of Naval Research and the National Science Foundation. This is WHOI contribution number 10941.

References

Arhan, M., Colin de Verdiere, A., Memery, L., 1994. The eastern boundary of the subtropical North Atlantic. Journal of Physical Oceanography 24, 1295–1316.

Antonov, J., Levitus, S., Boyer, T. P., Conkright, M., O'Brien, T., Stephens, C., 1998. World Ocean Atlas 1998 Vol. 1: Temperature of the Atlantic Ocean. NOAA Atlas NESDIS 27, U.S. Gov. Printing Office, Washington, D.C., 166 pp.

Batchelor, G. K., 1953. The Theory of Homogeneous Turbulence. Cambridge University Press, Cambridge, England, 197 pp.

Bersch, M., Meincke, J., Sy, A., 1999. Interannual thermohaline changes in the northern North Atlantic 1991–1996. Deep-Sea Research II 46, 55–75.

Böning, C. W., 1988. Characteristics of particle dispersion in the North Atlantic: an alternative interpretation of SOFAR float results. Deep-Sea Research I 35, 1379–1385.

Bower, A. S., Le Cann, B., Rossby, T., Zenk, W., Gould, J., Speer, K., Richardson, P. L., Prater, M. D., Zhang, H.-M., 2002. Directly measured mid-depth circulation in the northeastern North Atlantic Ocean. Nature 419, 603–607.

Boyer, T. P., Levitus, S., Antonov, J., Conkright, M., O'Brien, T., Stephens, C., 1998. World Ocean Atlas 1998 Vol. 4: Salinity of the Atlantic Ocean. NOAA Atlas NESDIS 30, U.S. Gov. Printing Office, Washington, D.C., 166 pp.

Bracco, A., Pedlosky, J., 2003. Vortex generation by topography in locally unstable baroclinic flows. Journal of Physical Oceanography 33, 207–219.

Bretherton, F. P., Davis, R. E., Fandry, C. B., 1976. A technique for objective analysis and design of oceanographic experiments applied to MODE-73. Deep-Sea Research 23, 559–582.

Carr, M.-E., Rossby, H. T., 2001. Pathways of the North Atlantic Current from surface drifters and subsurface floats. Journal of Geophysical Research 106, 4405–4419.

Cunningham, S. A., Haine, T. W. N., 1995. Labrador Sea Water in the eastern North Atlantic. Part I: A synoptic circulation inferred from a minimum in potential vorticity. Journal of Physical Oceanography 25, 649–665.

Cuny, J., Rhines, P. B., Niiler, P. P., Bacon, S., 2002. Labrador Sea boundary currents and the fate of the Irminger Sea Water. Journal of Physical Oceanography 32, 627–647.

Curry, R., 2003. HydroBase 2.0: A Database of Hydrographic Profiles and Tools for Climatological Analysis. Woods Hole Oceanographic Institution Technical Report, Woods Hole, 80 pp., in press.

Davis, R. E., 1991. Observing the general circulation with floats. Deep-Sea Research 38 (Suppl. 1), S531–S571.

Davis, R. E., Webb, D. C., Regier, L. A., Dufour, J., 1992. The Autonomous Lagrangian Circulation Explorer (ALACE). Journal of Atmospheric and Oceanic Technology 9, 264–285.

Davis, R. E., 1998. Preliminary results from directly measuring middepth circulation in the tropical and South Pacific. Journal of Geophysical Research 103, 24,619–24,639.

Davis, R. E., Sherman, J. T., Dufour, J., 2001. Profiling ALACEs and other advances in autonomous subsurface floats. Journal of Atmospheric and Oceanic Technology 18, 982–993.

DeGroot, M. H., 1989. Probability and Statistics. Addison-Wesley, Reading, MA, 723 pp.

Eden, C., Böning, C., 2002. Sources of eddy kinetic energy in the Labrador Sea. Journal of Physical Oceanography 32, 3346–3363.

Fofonoff, N. P., 1969. Spectral characteristics of internal waves in the ocean. Deep-Sea Research 16, 58–71.

Fratantoni, D. M., 2001. North Atlantic surface circulation during the 1990's observed with satellite-tracked drifters. Journal of Geophysical Research 106, 22,067–22,093.

Freeland, H. J., Rhines, P. B., Rossby, T., 1975. Statistical observations of the trajectories of neutrally buoyant floats in the North Atlantic. Journal of Marine Research 33, 383–404.

Lab Sea Group, 1998. The Labrador Sea Deep Convection Experiment. Bulletin of the American Meteorological Society 79, 2033–2058.

LaCasce, J. H., 2000. Floats and f/H. Journal of Marine Research 58, 61–95.

Lavender, K. L., Davis, R. E., Owens, W. B., 2000. Mid-depth recirculation observed in the interior Labrador and Irminger Seas by direct velocity measurements. Nature 407, 66–69.

Lavender, K. L., Davis, R. E., Owens, W. B., 2002. Observations of open-ocean deep convection in the Labrador Sea from subsurface floats. Journal of Physical Oceanography 32, 511–526.

Lazier, J. R. N., 1973. The renewal of Labrador Sea Water. Deep-Sea Research 20, 341–353.

Levitus, S., Boyer, T. P., 1994. World Ocean Atlas 1994 Volume 4: Temperature. NOAA Atlas NESDIS 4, U.S. Department of Commerce, Washington, D.C., 117 pp.

Levitus, S., Burgett, R., Boyer, T. P., 1994. World Ocean Atlas 1994 Volume 3: Salinity. NOAA Atlas NESDIS 3, U.S. Department of Commerce, Washington, D.C., 99 pp.

Lilly, J. M., Rhines, P. B., Visbeck, M., Davis, R., Lazier, J. R. N., Schott, F., Farmer, D., 1999. Observing deep convection in the Labrador Sea during winter 1994/95. Journal of Physical Oceanography 29, 2065–2098.

Lozier, M. S., Owens, W. B., Curry, R. G., 1995. The climatology of the North Atlantic. Progress in Oceanography 36, 1–44.

McCartney, M. S., Mauritzen, C., 2001. On the origin of the warm inflow to the Nordic Seas. Progress in Oceanography 51, 125–214.

McWilliams, J. C., LDE Group, 1983. The local dynamics of eddies in the western North Atlantic. In: Robinson, A. R. (Ed.), Eddies in Marine Science. Springer-Verlag, Berlin, pp. 92–113.

Molinari, R. L., Fine, R. A., Wilson, W. D., Curry, R. G., Abell, J., McCartney, M. S., 1998. The arrival of recently formed Labrador Sea Water in the deep western boundary current at 26.5°N. Geophysical Research Letters 25, 2249–2252.

Pickart, R. S., Torres, D. J., Clarke, R. A., 2002. Hydrography of the Labrador Sea during active convection. Journal of Physical Oceanography 32, 428–457.

Pickart, R. S., Straneo, F., Moore, G. W. K., 2003. Is Labrador Sea Water formed in the Irminger basin? Deep-Sea Research I 50, 23–52.

Pingree, R. D., Le Cann, B., 1990. Structure, strength and seasonality of the slope currents in the Bay of Biscay region. Journal of the Marine Biological Association of the United Kingdom 70, 857–885.

Prater, M. D., 2002. Eddies in the Labrador Sea as observed by profiling RAFOS floats and remote sensing. Journal of Physical Oceanography 32, 411–427.

Reid, J. L., 1994. On the total geostrophic circulation of the North Atlantic Ocean: Flow patterns, tracers, and transports. Progress in Oceanography 33, 1–92.

Rossby, H. T., Riser, S. C., Mariano, A. J., 1983. The western North Atlantic – a Lagrangian viewpoint. In: Robinson, A. R. (Ed.), Eddies in Marine Science, Springer-Verlag, Berlin, pp. 66–91.

Smith, W. H. F., Sandwell, D. T., 1997. Global sea floor topography from satellite altimetry and ship depth soundings. Science 277, 1956–1962.

Spall, M. A., Pickart, R. S., 2003. Wind-driven recirculations and exchange in the Labrador and Irminger Seas. Journal of Physical Oceanography 33, 1829–1845.

Sy, A., Rhein, M., Lazier, J. R. N., Koltermann, K. P., Meincke, J., Putzka, A., Bersch, M., 1997. Surprisingly rapid spreading of newly formed intermediate waters across the North Atlantic Ocean. Nature 386, 675–679.

Talley, L. D., McCartney, M. S., 1982. Distribution and circulation of Labrador Sea Water. Journal of Physical Oceanography 12, 1189–1205.

Taylor, G. I., 1921. Diffusion by continuous movements. Proceedings of the London Mathematical Society 20, 196–212.

White, M. A., Heywood, K. J., 1995. Seasonal and interannual changes in the North Atlantic subpolar gyre from Geosat and TOPEX/POSEIDON altimetry. Journal of Geophysical Research 100, 24,931–24,941.

Figure Captions

Figure 1. Float deployment positions in the subpolar gyre, where symbol type indicates year of deployment between November 1994 and February 1998. The concentrated deployment of floats in the western Labrador Sea was a component of the Labrador Sea Deep Convection Experiment, and the broad-scale deployments coincide with WOCE hydrographic transects. From light to dark gray, shading indicates bathymetry < 4000 m, < 3000 m, < 2000 m, < 1000 m, and < 500 m depth.

Figure 2. The number of subsurface displacements (N) in a nominal 110 km square grid. The highest density of observations is in the Labrador Sea because of concentrated float deployments there, although the entire North Atlantic basin north of 44°N is well-sampled.

Figure 3. Complete trajectories of six floats that drifted cyclonically around the subpolar gyre. Each float is represented by one color. Each arrow represents the subsurface float displacement during one drift cycle, and the gap between arrows represents the 24-hour period of surface drift. The legend indicates the transit time and the average drift pressure of each float.

Figure 4. Trajectories of 33 floats drifting at 1500 m, the depth of convectively-formed Labrador Sea Water, after launch or entry into the Labrador Sea. No floats travelled south along the western boundary beyond 44°N.

Figure 5. Complete trajectories of eight floats that reached the Iceland-Faroe Rise from the northern North Atlantic. Six of these floats entered the Norwegian Sea. Pressure at drift depth ranged from 5–1160 db.

Figure 6. Space-time averages of drift velocity data in bins roughly 110 km square. Velocity is shown as displacement vectors, with red arrows indicating speeds faster than 5 cm s^{-1}. Only averages containing more than three observations are plotted. Prior to averaging, data from depths between 200–1800 m were adjusted to 700 m depth using geostrophic shear computed from the HydroBase 2.0 climatology.

Figure 7. Single-particle Lagrangian time-lagged autocovariances, computed for each float and then averaged according to drift depth. Measurements are essentially uncorrelated after 10 days at all depths, and the Lagrangian integral time scale is between 6 and 10 days. Velocity statistics are isotropic at all depths.

Figure 8. Space-time averages of drift velocity data as in Figure 6, and the estimated sampling error assuming an integral time scale of 10 days. Errors are plotted as ellipses in which the length of the semi-axes are scaled to the standard deviation of the principal axes of the error covariance. Only estimates whose mean exceeds the error are plotted. In all but a few averages (all in boundary currents) the variance far exceeds the mean, however the density of observations yields statistically significant sample mean velocities for most estimates.

Figure 9. Estimated array bias arising from an unequal distribution of floats throughout the domain. The array bias velocity is shown as displacement vectors, with red arrows indicating speeds faster than 5 cm s^{-1}. The estimated bias produces an artificial divergent flow from the deployment region in the western Labrador Sea, and larger values near Flemish Cap (47°N, 45°W) where eddy variability is extremely high. However, the magnitudes are typically smaller than the estimated statistical error.

Figure 10. Space-lagged correlations of drift velocities adjusted to 700 m depth, plotted versus lag in x and y. a) Correlation of zonal velocity. b) Correlation of meridional velocity. The covariances were calculated for drift velocities measured within an integral time scale (10 days) of one another. Averages, $< >$, were computed over all time in bins defined by zonal (x) and meridional (y) separation, and correlations were normalized by the value at zero lag. Contour interval is 0.1, and positive correlations are shaded in gray.

Figure 11. Cross-sections of space-lagged covariances of drift velocities in Figure 10 at zero-lag in the normal coordinate. The shape of the curves is consistent with 2-D isotropic turbulence in a non-divergent flow.

Figure 12. Space-lagged covariances of drift velocity components parallel ($u_\parallel$) and normal ($u_\perp$) to the local contour of barotropic potential vorticity, $\zeta = f/H$. The

covariances along constant ζ are plotted versus spatial separation. Drift velocities were adjusted to 700 m depth, and averages were computed in bins defined by the total separation distance and the change in local ζ between observations.

Figure 13. Objectively mapped mean circulation at 700 m depth in regions where map skill is greater than 0.7, which corresponds to an estimated uncertainty of 4.1 cm in pressure (see text). a) Geostrophic pressure measured in centimeters of water. Contour interval is 1 cm; 'L's and 'H's mark selected low and high pressure centers, respectively. Bathymetry shallower than 700 m is shaded. b) Geostrophic velocity plotted as displacement vectors as in Figure 6. Bathymetry is shaded as in Figure 1.

Figure 14. Trajectories of floats that a) travelled east from the Labrador Sea to the Irminger Sea just south of the tip of Greenland. b) looped cyclonically in and out of the West Greenland Current. c) looped cyclonically in and out of the Labrador Current. Each figure contains displacements at a range of drift depths. Note that scales vary between figures, and stars indicate either the deployment position or the start of the first complete displacement in the region plotted.

Figure 15. Objectively mapped mean circulation plotted as contours of geostrophic pressure where map skill is greater than 0.5 at a) 400 m depth. b) 1500 m depth. Thick red contour indicates map skill equal to 0.7. Corresponding uncertainties in pressure for map skill of 0.5 (0.7) are 7.9 (6.1) cm at 400 m depth, and 4.1 (3.2) cm at 1500 m depth. Bathymetry shallower than map depth is shaded. Contour interval for pressure is 1 cm, and color scales differ between plots.

Figure 16. Comparison of the geostrophic velocity at 400 m relative to 1500 m depth along a cross-basin transect in the Labrador Sea (see inset). The geostrophic velocity computed from a 10-year average of hydrographic data (thin line) is compared to the difference of the objectively mapped velocity fields at 400 m and 1500 m depth (thick line). Dotted lines indicate the 95% confidence interval on the map estimate. Positive values indicate that relative to 1500 m, the flow at 400 m is to the southeast.

Figure 17. Eddy kinetic energy ($cm^2\ s^{-2}$) in the subpolar North Atlantic. EKE was estimated from departures of drift velocity data (adjusted to 700 m depth) from space-time averaged velocities that were locally smoothed (see text). Contour interval is 25 $cm^2\ s^{-2}$.

Figure 18. Active deep convection observed in the cyclonic recirculation southwest of the tip of Greenland from January–March, 2001. a) Nine-day float displacements at an average drift pressure of 640 db. Circles mark locations of temperature profiles. b) Profiles of potential temperature versus pressure measured while the float ascended to the surface at the end of its nine-day drift cycle. Progressive cooling and deepening of the mixed layer from roughly 300 m to 1100 m depth was observed over a period of weeks while the float drifted in the cyclonic gyre just offshore of the West Greenland Current.

	$\Phi = \infty$	$\Phi = 1$
Signal-to-noise ratio	7.20	7.85
Correlation with data	0.93	0.93
Maximum speed (cm s^{-1})		
East Greenland Current	15.58	16.96
West Greenland Current	18.06	19.47
Labrador Current	12.03	12.39

Table 1: Comparison of properties of objective maps computed with varied dependence on $\zeta = f/H$, as determined by the parameter Φ.

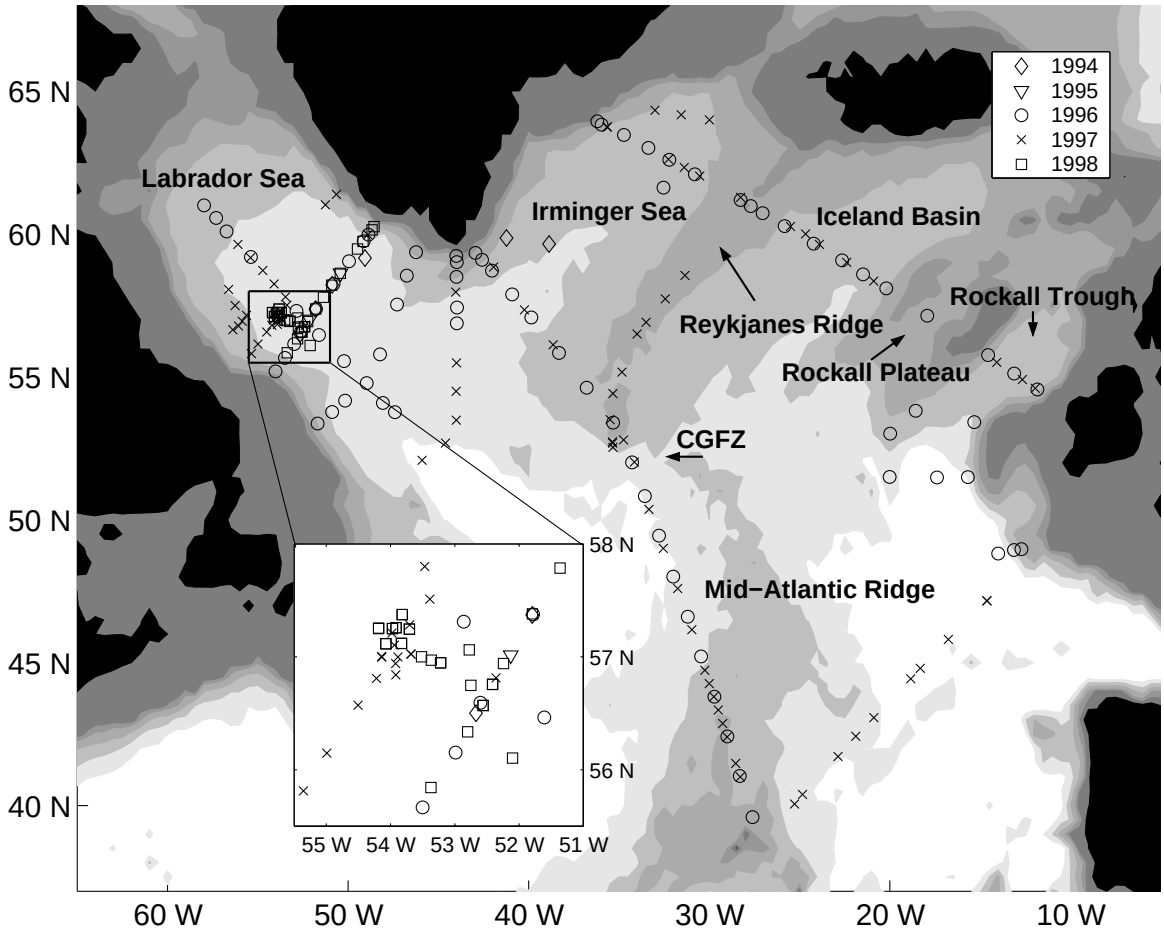

Figure 1: Float deployment positions in the subpolar gyre, where symbol type indicates year of deployment between November 1994 and February 1998. The concentrated deployment of floats in the western Labrador Sea was a component of the Labrador Sea Deep Convection Experiment, and the broad-scale deployments coincide with WOCE hydrographic transects. From light to dark gray, shading indicates bathymetry < 4000 m, < 3000 m, < 2000 m, < 1000 m, and < 500 m depth.

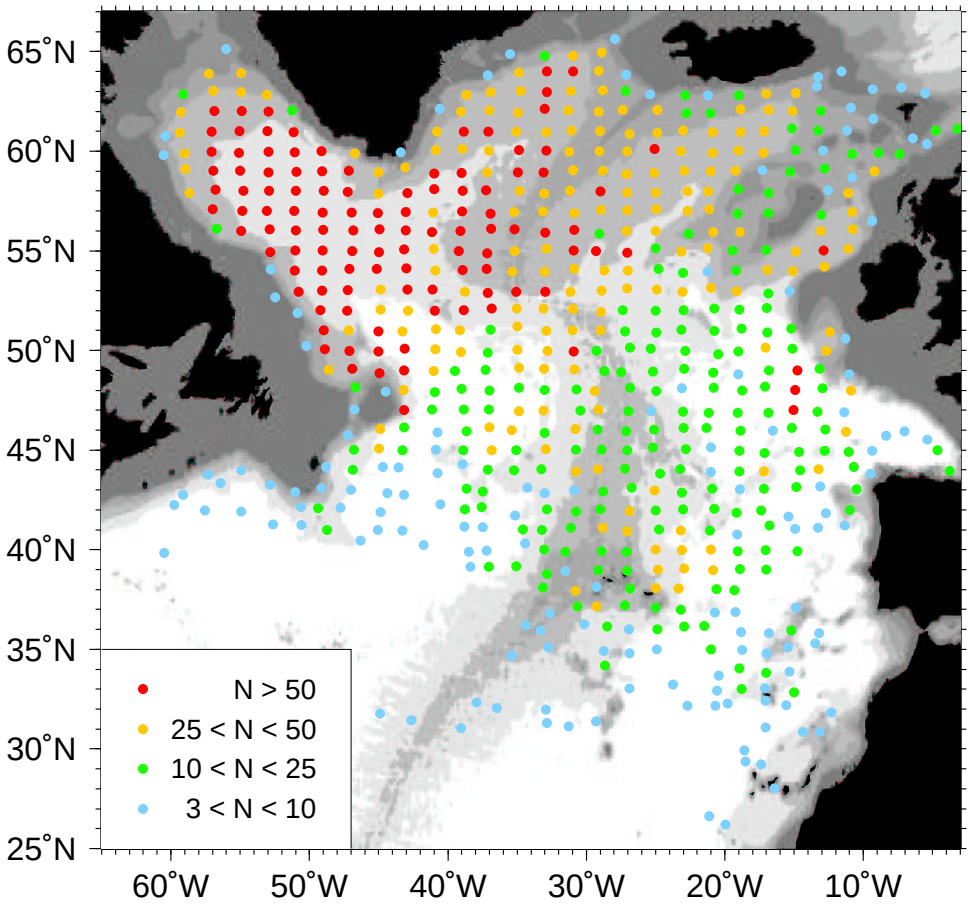

Figure 2: The number of subsurface displacements (N) in a nominal 110 km square grid. The highest density of observations is in the Labrador Sea because of concentrated float deployments there, although the entire North Atlantic basin north of 44°N is well-sampled.

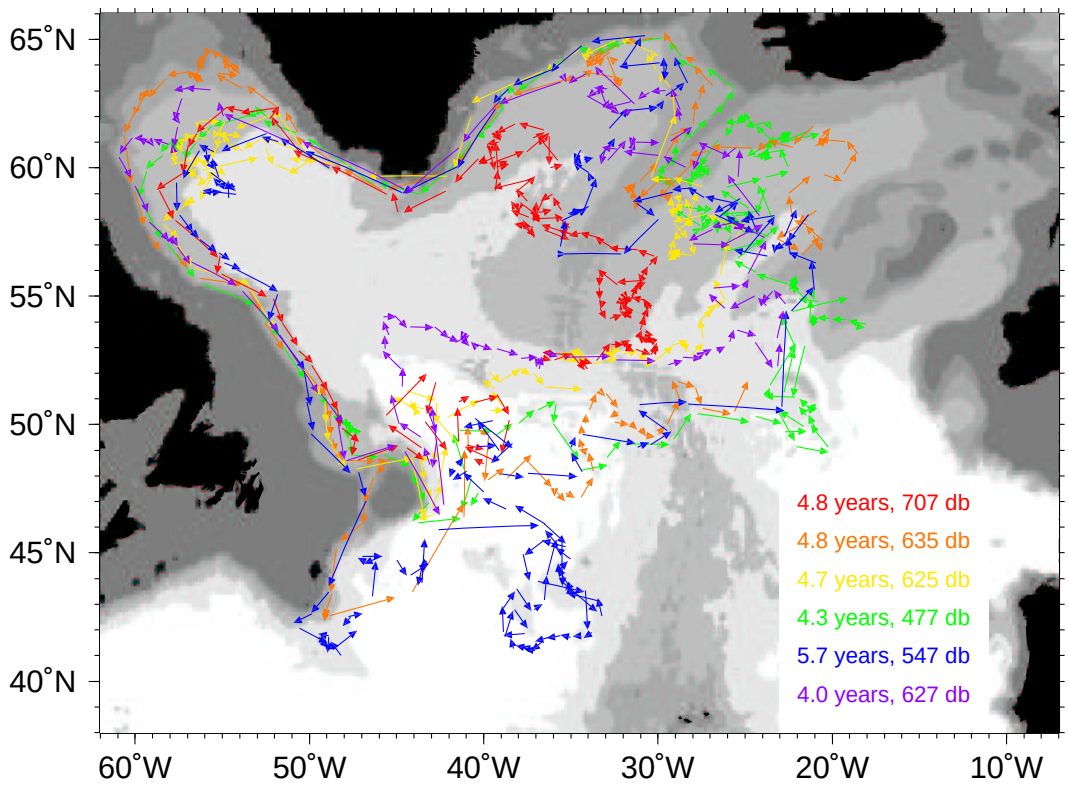

Figure 3: Complete trajectories of six floats that drifted cyclonically around the subpolar gyre. Each float is represented by one color. Each arrow represents the subsurface float displacement during one drift cycle, and the gap between arrows represents the 24-hour period of surface drift. The legend indicates the transit time and the average drift pressure of each float.

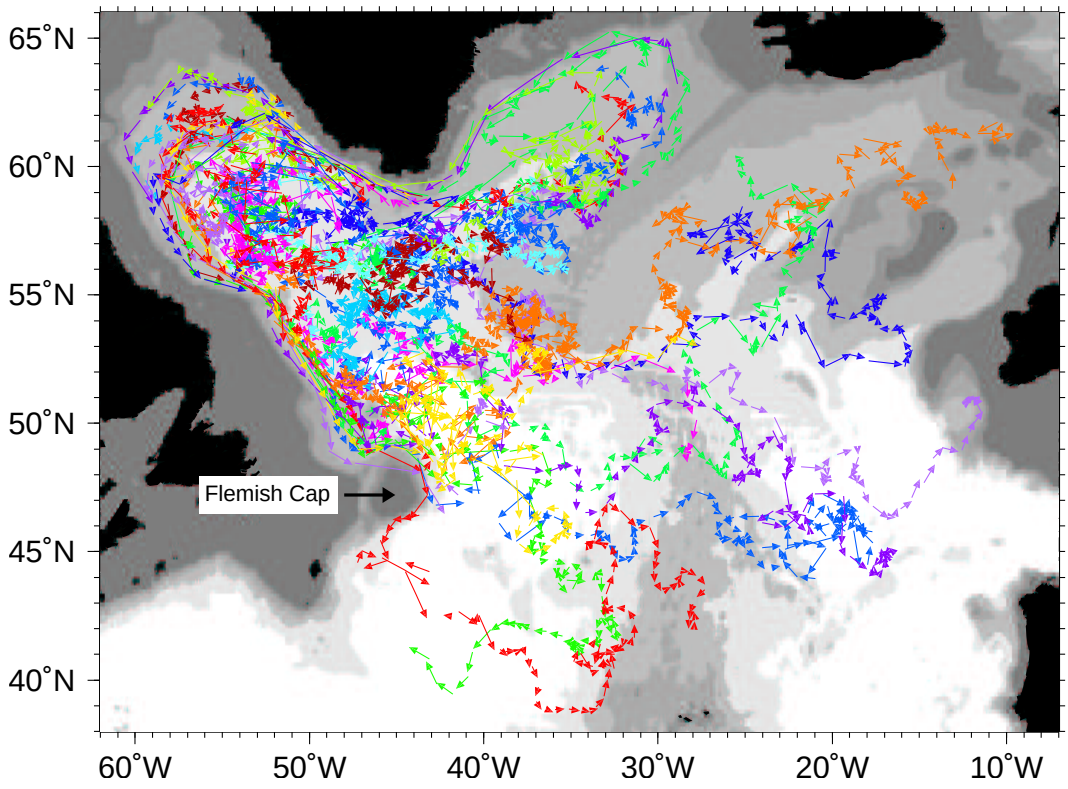

Figure 4: Trajectories of 33 floats drifting at 1500 m, the depth of convectively-formed Labrador Sea Water, after launch or entry into the Labrador Sea. No floats travelled south along the western boundary beyond 44°N.

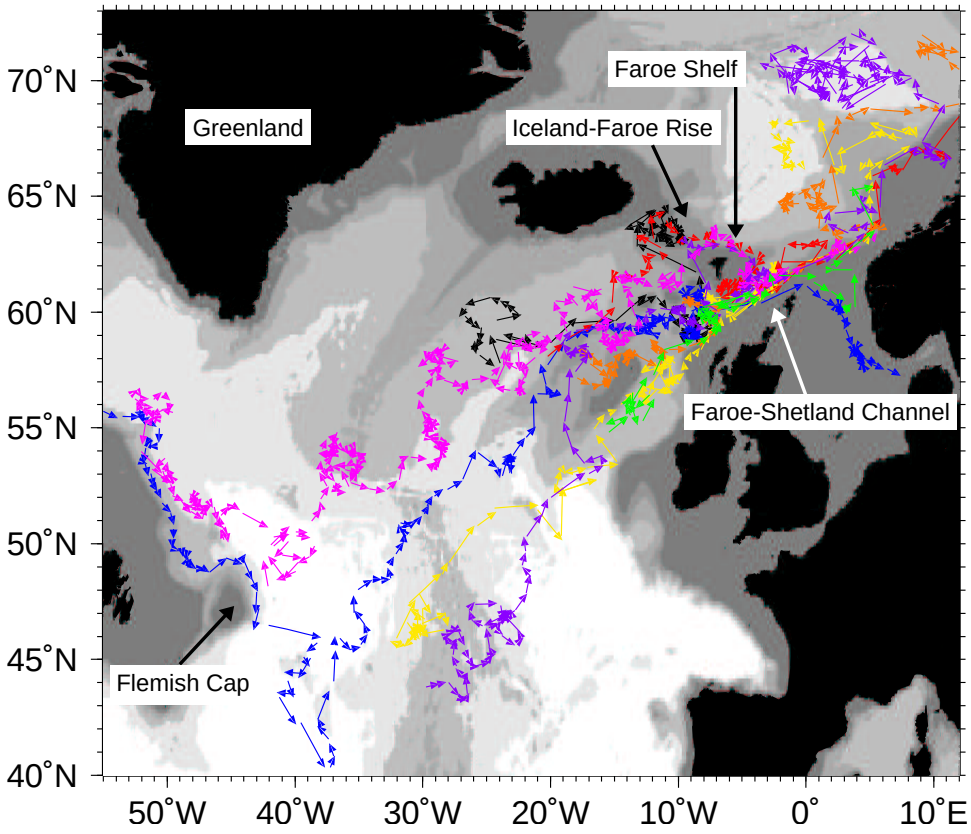

Figure 5: Complete trajectories of eight floats that reached the Iceland-Faroe Rise from the northern North Atlantic. Six of these floats entered the Norwegian Sea. Pressure at drift depth ranged from 5–1160 db.

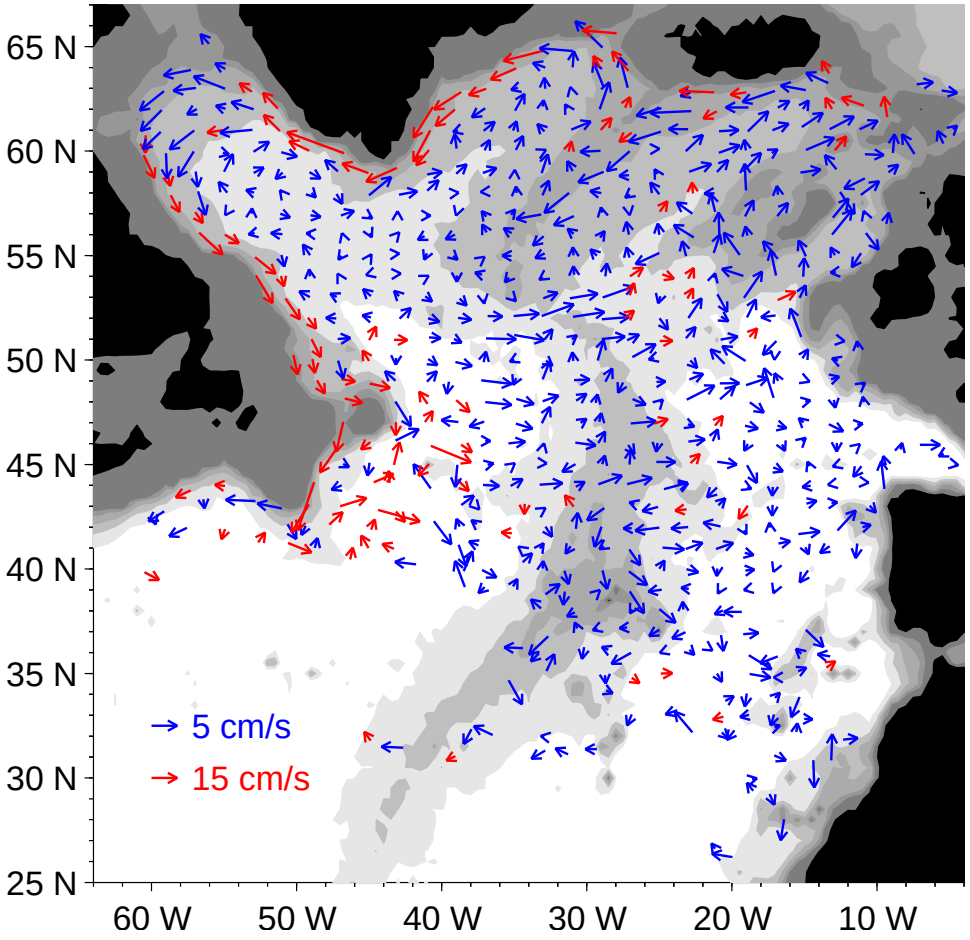

Figure 6: Space-time averages of drift velocity data in bins roughly 110 km square. Velocity is shown as displacement vectors, with red arrows indicating speeds faster than 5 cm s^{-1}. Only averages containing more than three observations are plotted. Prior to averaging, data from depths between 200–1800 m were adjusted to 700 m depth using geostrophic shear computed from the HydroBase 2.0 climatology.

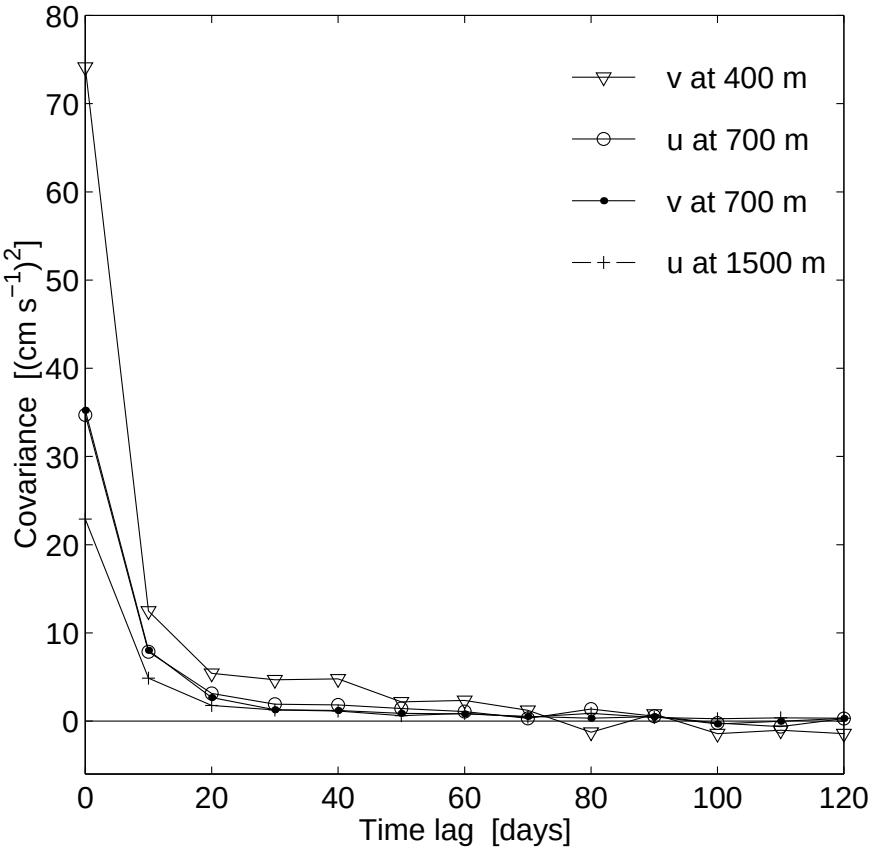

Figure 7: Single-particle Lagrangian time-lagged autocovariances, computed for each float and then averaged according to drift depth. Measurements are essentially uncorrelated after 10 days at all depths, and the Lagrangian integral time scale is between 6 and 10 days. Velocity statistics are isotropic at all depths.

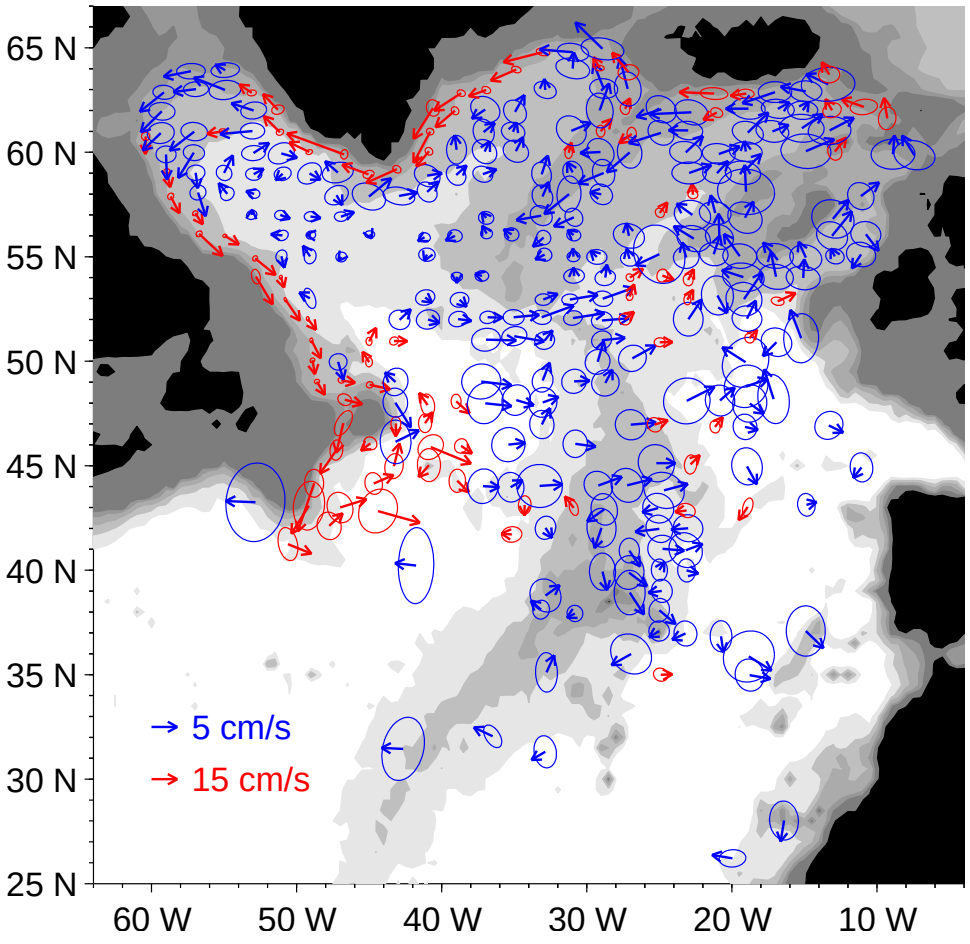

Figure 8: Space-time averages of drift velocity data as in Figure 6, and the estimated sampling error assuming an integral time scale of 10 days. Errors are plotted as ellipses in which the length of the semi-axes are scaled to the standard deviation of the principal axes of the error covariance. Only estimates whose mean exceeds the error are plotted. In all but a few averages (all in boundary currents) the variance far exceeds the mean, however the density of observations yields statistically significant sample mean velocities for most estimates.

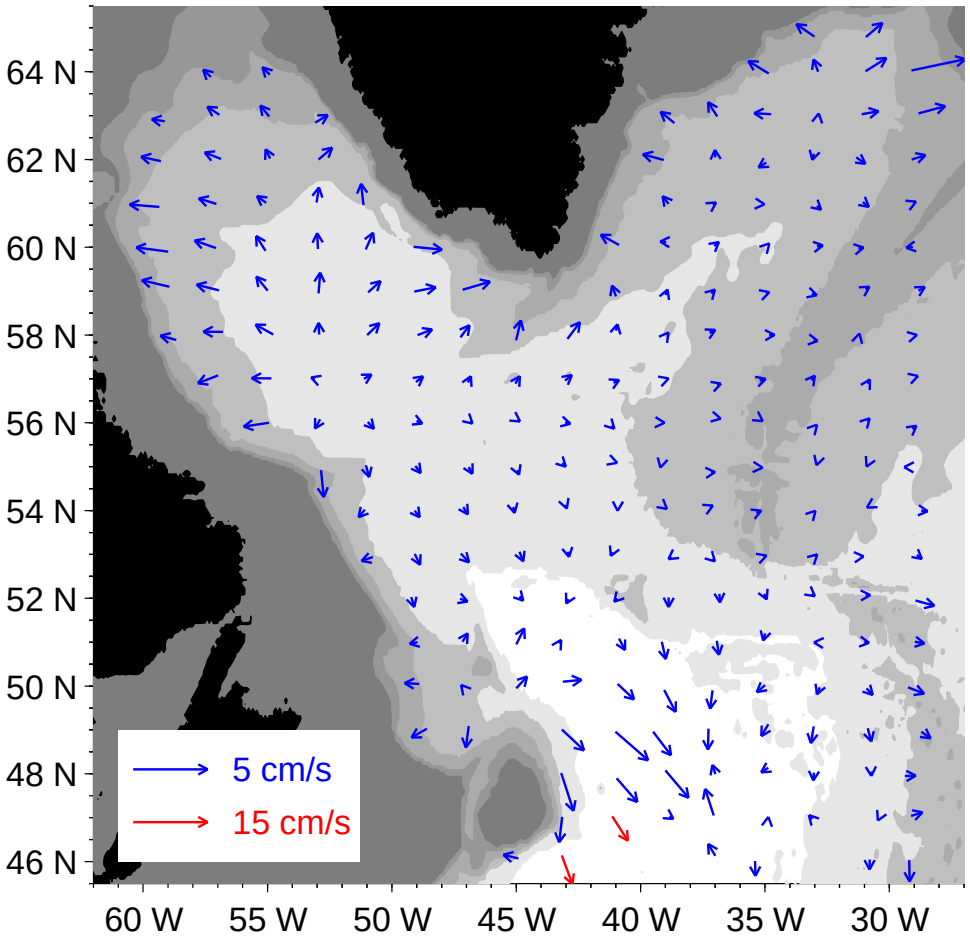

Figure 9: Estimated array bias arising from an unequal distribution of floats throughout the domain. The array bias velocity is shown as displacement vectors, with red arrows indicating speeds faster than 5 cm s^{-1}. The estimated bias produces an artificial divergent flow from the deployment region in the western Labrador Sea, and larger values near Flemish Cap (47°N, 45°W) where eddy variability is extremely high. However, the magnitudes are typically smaller than the estimated statistical error.

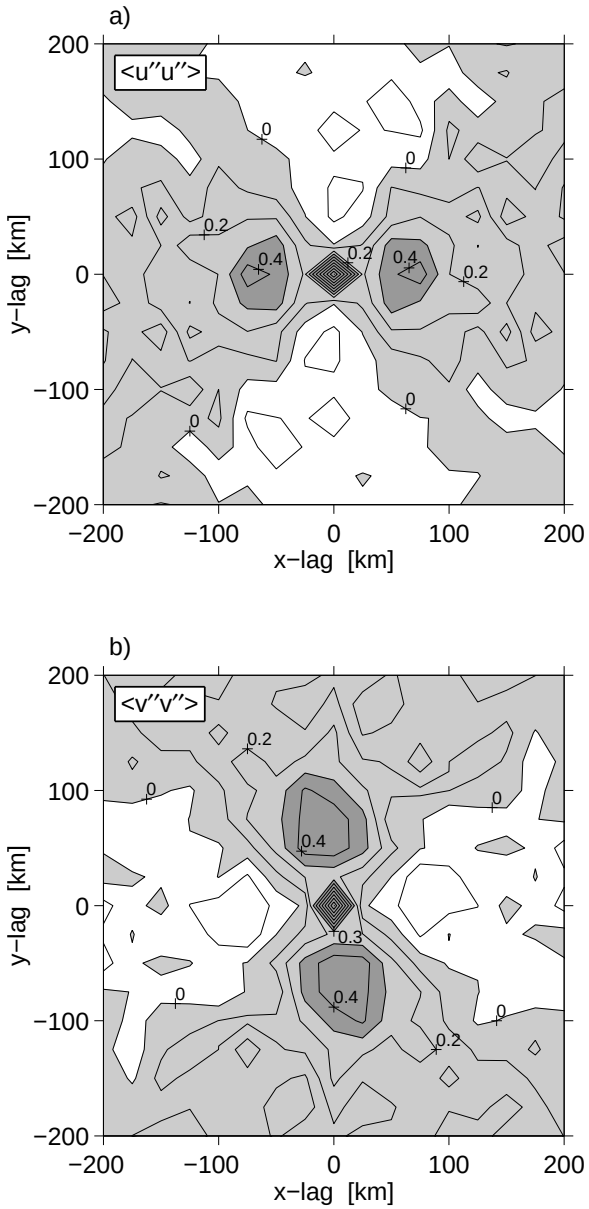

Figure 10: Space-lagged correlations of drift velocities adjusted to 700 m depth, plotted versus lag in x and y. a) Correlation of zonal velocity. b) Correlation of meridional velocity. The covariances were calculated for drift velocities measured within an integral time scale (10 days) of one another. Averages, $< >$, were computed over all time in bins defined by zonal (x) and meridional (y) separation, and correlations were normalized by the value at zero lag. Contour interval is 0.1, and positive correlations are shaded in gray.

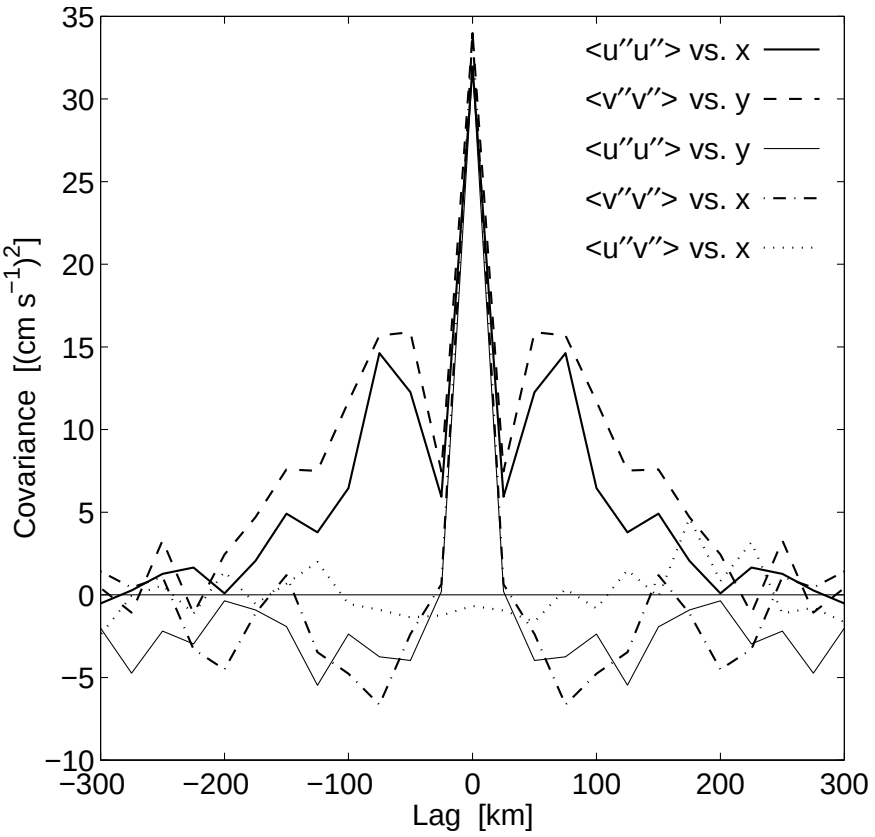

Figure 11: Cross-sections of space-lagged covariances of drift velocities in Figure 10 at zero-lag in the normal coordinate. The shape of the curves is consistent with 2-D isotropic turbulence in a non-divergent flow.

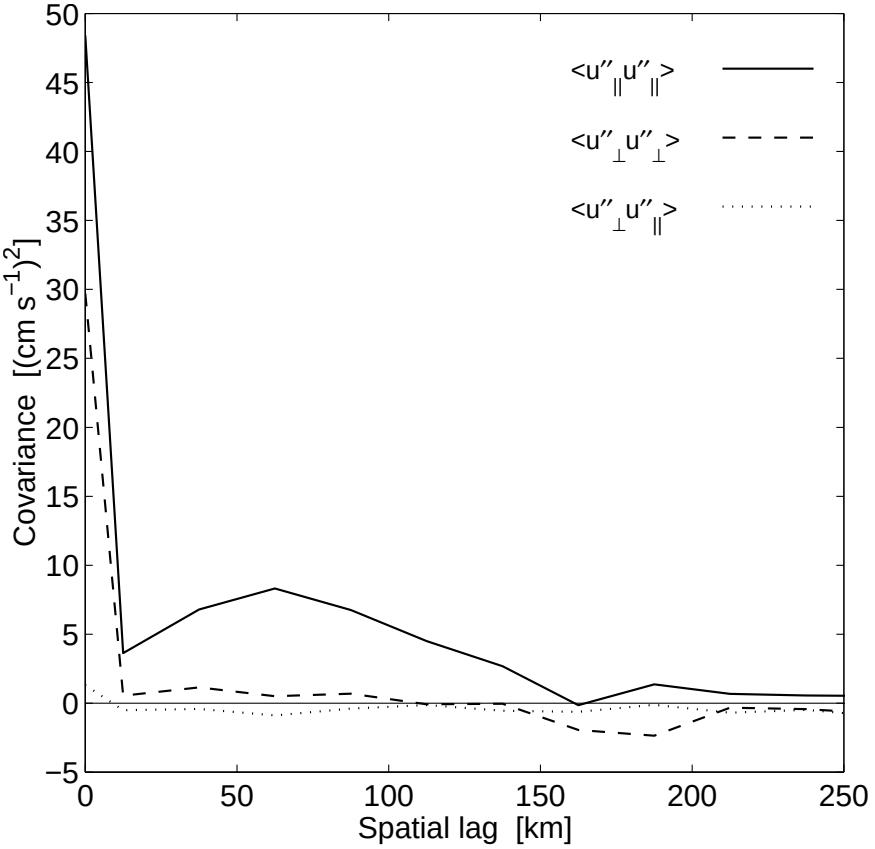

Figure 12: Space-lagged covariances of drift velocity components parallel ($u_{\parallel}$) and normal ($u_{\perp}$) to the local contour of barotropic potential vorticity, $\zeta = f/H$. The covariances along constant ζ are plotted versus spatial separation. Drift velocities were adjusted to 700 m depth, and averages were computed in bins defined by the total separation distance and the change in local ζ between observations.

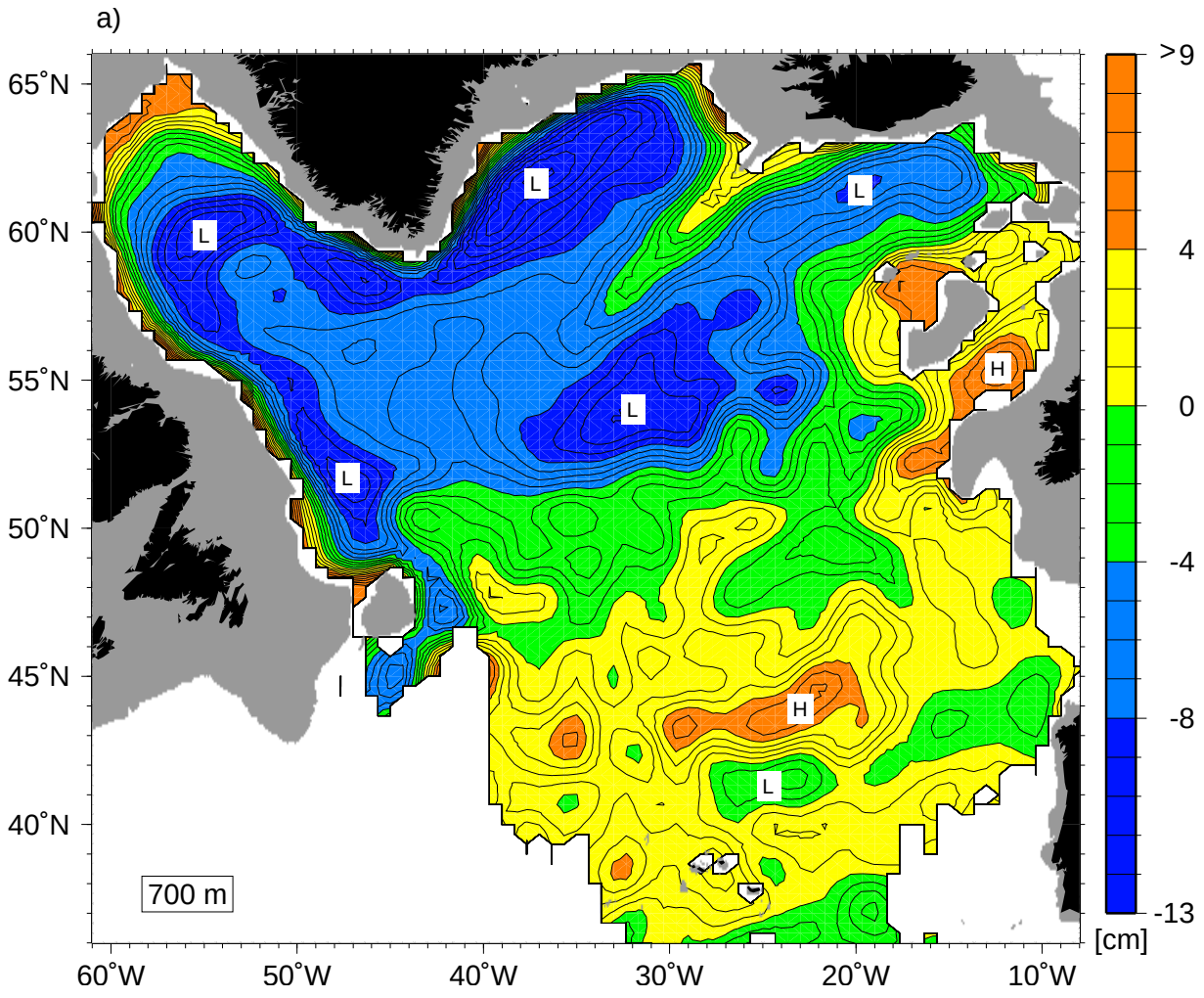
a)
65˚N
60˚N
55˚N
50˚N
45˚N
40˚N
60˚W
50˚W
40˚W
30˚W
20˚W
10˚W
L
L
L
L
L
L
H
H
L
700 m
>9
4
0
-4
-8
-13
[cm]

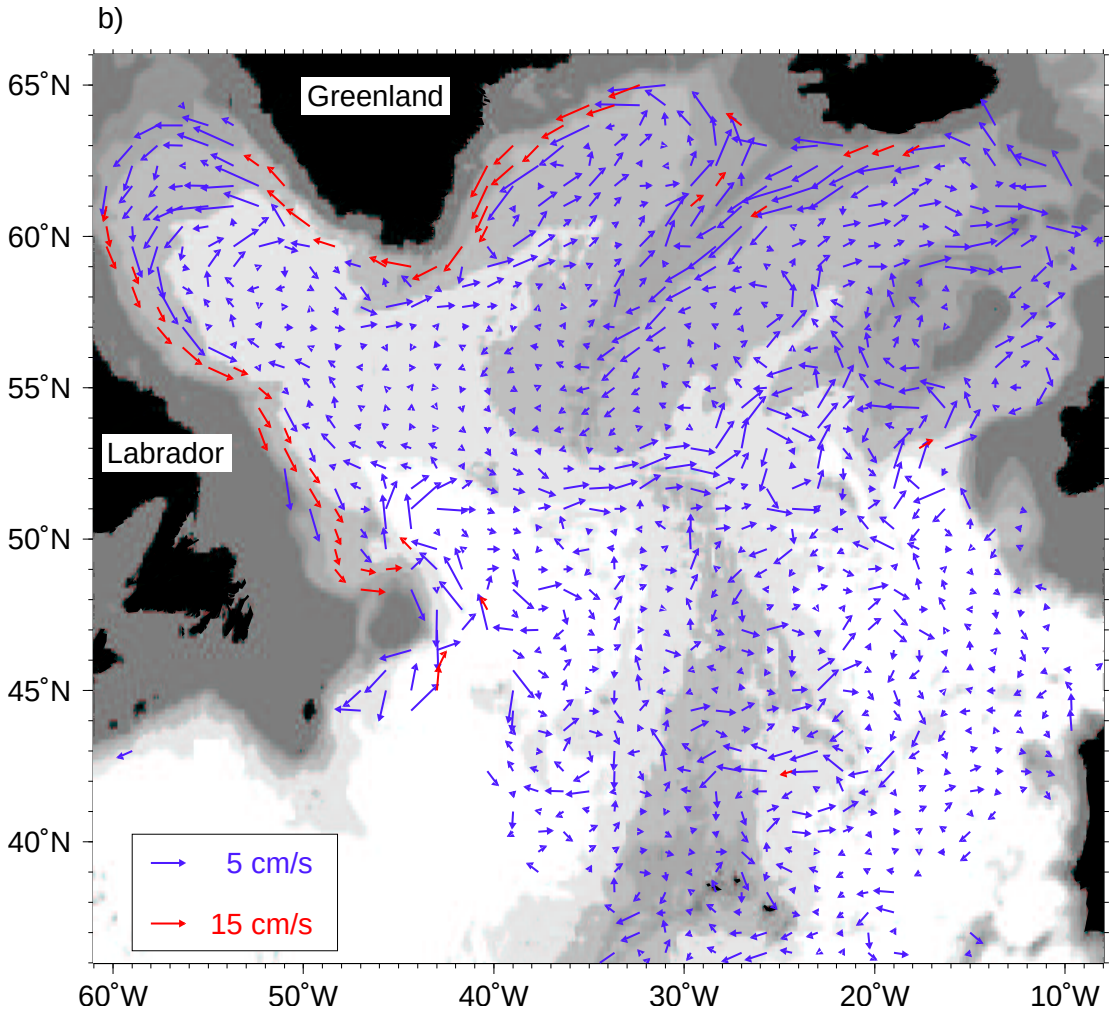

Figure 13: Objectively mapped mean circulation at 700 m depth in regions where map skill is greater than 0.7, which corresponds to an estimated uncertainty of 4.1 cm in pressure (see text). a) Geostrophic pressure measured in centimeters of water. Contour interval is 1 cm; 'L's and 'H's mark selected low and high pressure centers, respectively. Bathymetry shallower than 700 m is shaded. b) Geostrophic velocity plotted as displacement vectors as in Figure 6. Bathymetry is shaded as in Figure 1.

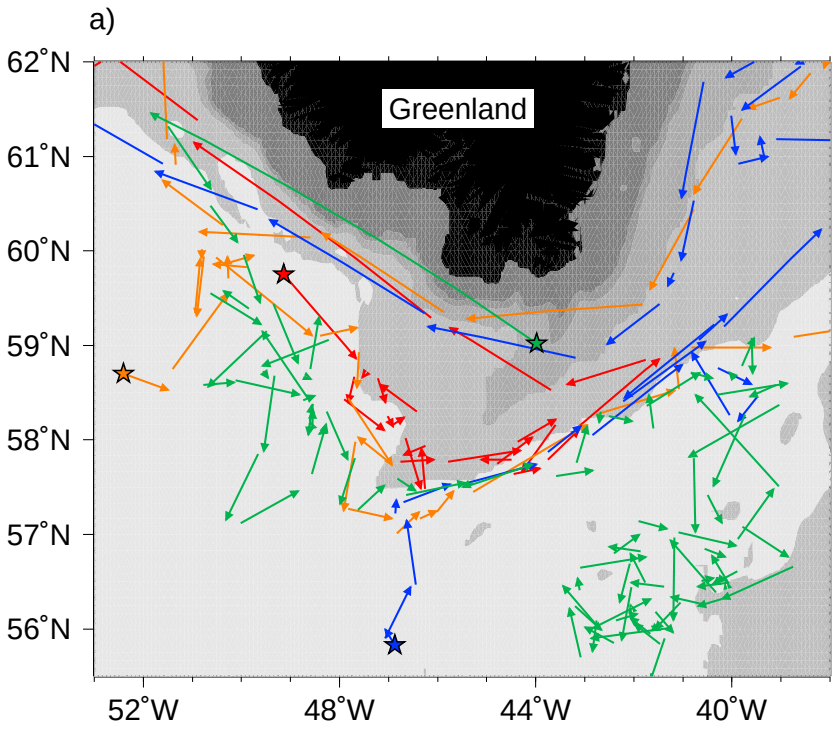
a)
Greenland
62˚N
61˚N
60˚N
59˚N
58˚N
57˚N
56˚N
52˚W
48˚W
44˚W
40˚W

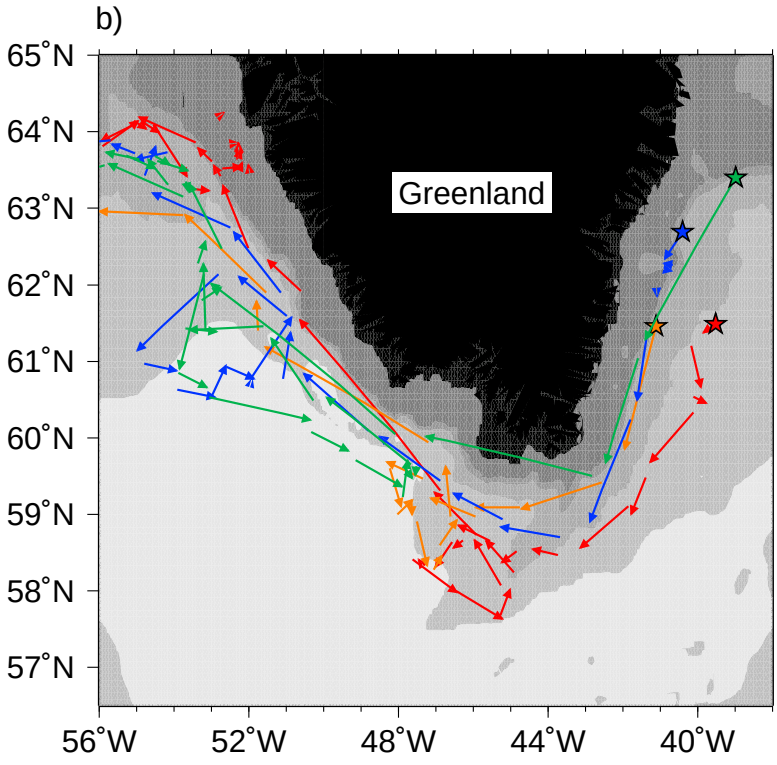
b)
Greenland
65˚N
64˚N
63˚N
62˚N
61˚N
60˚N
59˚N
58˚N
57˚N
56˚W
52˚W
48˚W
44˚W
40˚W

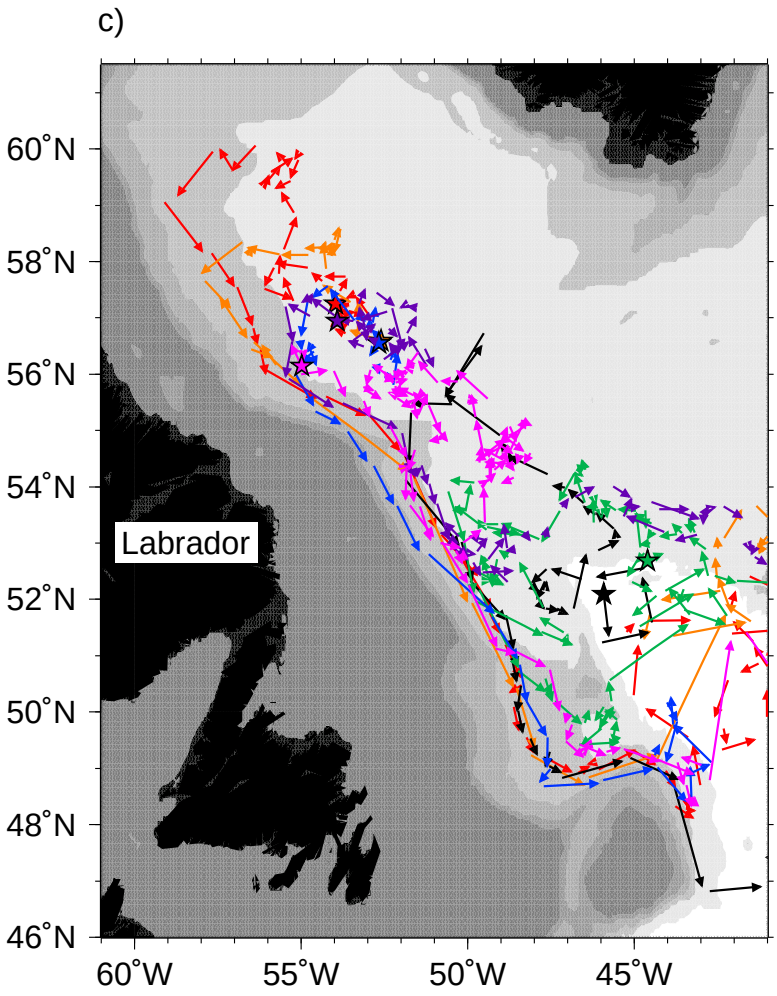

Figure 14: Trajectories of floats that a) travelled east from the Labrador Sea to the Irminger Sea just south of the tip of Greenland. b) looped cyclonically in and out of the West Greenland Current. c) looped cyclonically in and out of the Labrador Current. Each figure contains displacements at a range of drift depths. Note that scales vary between figures, and stars indicate either the deployment position or the start of the first complete displacement in the region plotted.

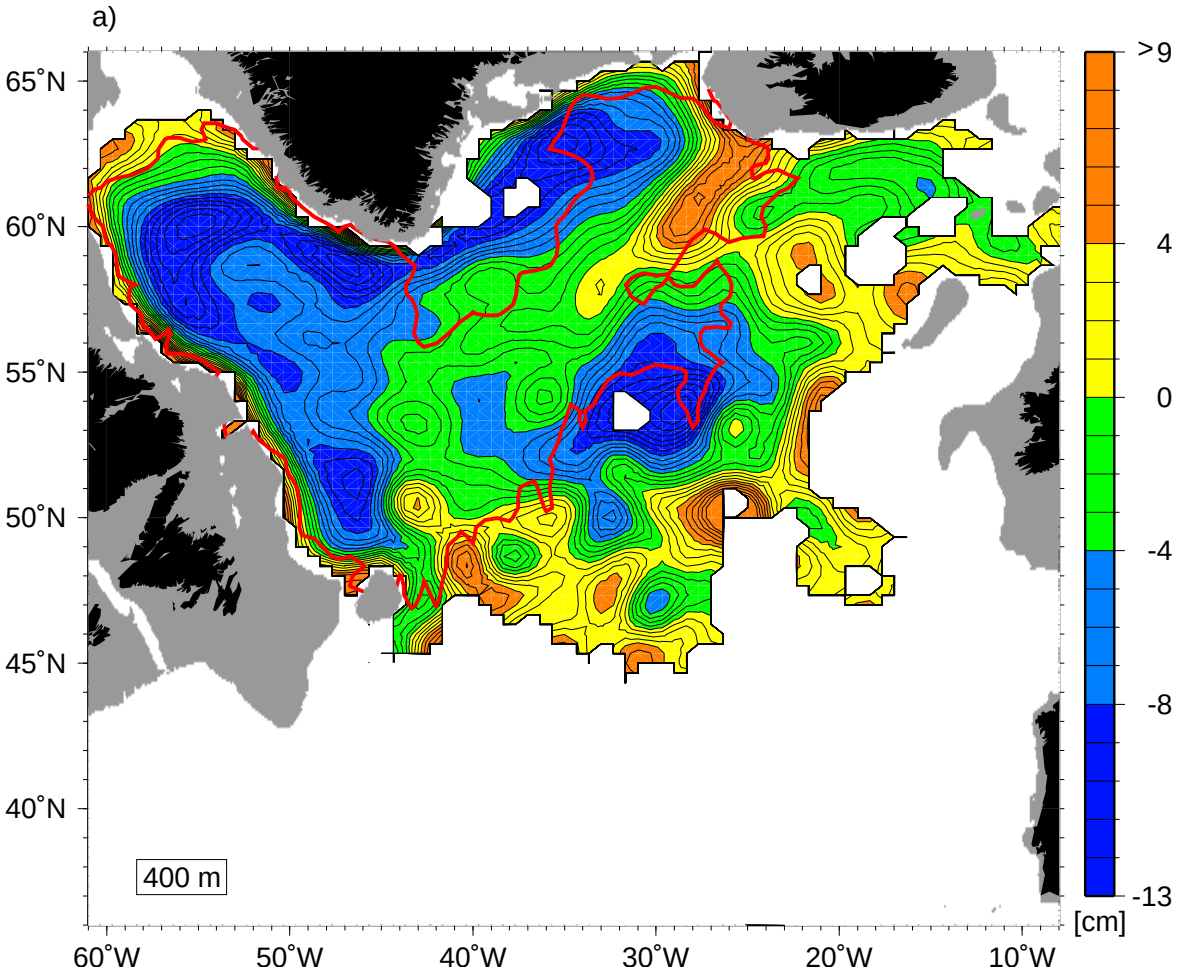
a)
65˚N
60˚N
55˚N
50˚N
45˚N
40˚N
60˚W
50˚W
40˚W
30˚W
20˚W
10˚W
400 m
>9
4
0
-4
-8
-13
[cm]

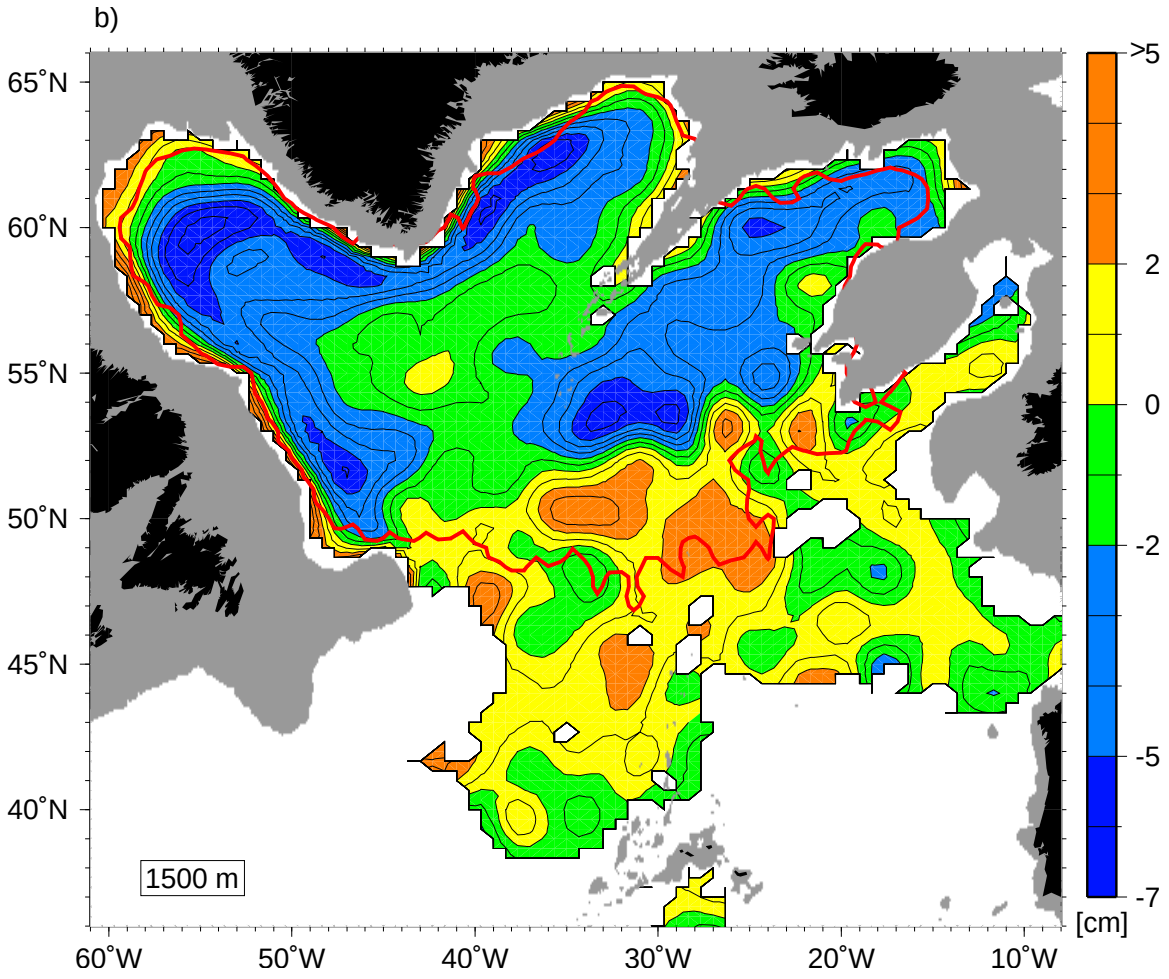

Figure 15: Objectively mapped mean circulation plotted as contours of geostrophic pressure where map skill is greater than 0.5 at a) 400 m depth. b) 1500 m depth. Thick red contour indicates map skill equal to 0.7. Corresponding uncertainties in pressure for map skill of 0.5 (0.7) are 7.9 (6.1) cm at 400 m depth, and 4.1 (3.2) cm at 1500 m depth. Bathymetry shallower than map depth is shaded. Contour interval for pressure is 1 cm, and color scales differ between plots.

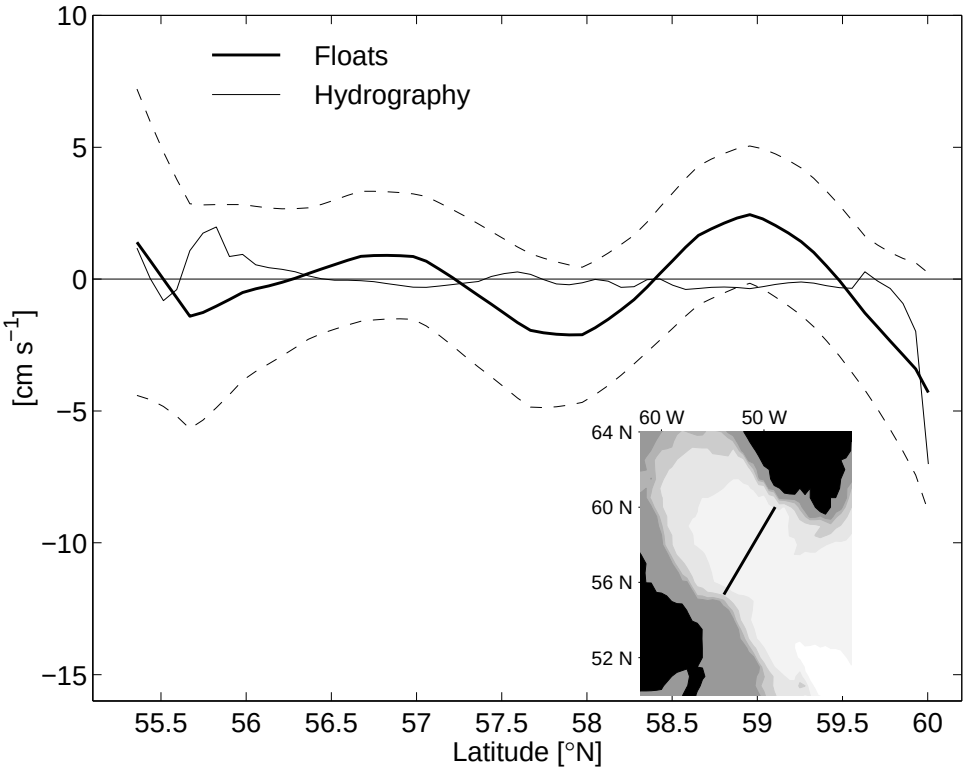

Figure 16: Comparison of the geostrophic velocity at 400 m relative to 1500 m depth along a cross-basin transect in the Labrador Sea (see inset). The geostrophic velocity computed from a 10-year average of hydrographic data (thin line) is compared to the difference of the objectively mapped velocity fields at 400 m and 1500 m depth (thick line). Dotted lines indicate the 95% confidence interval on the map estimate. Positive values indicate that relative to 1500 m, the flow at 400 m is to the southeast.

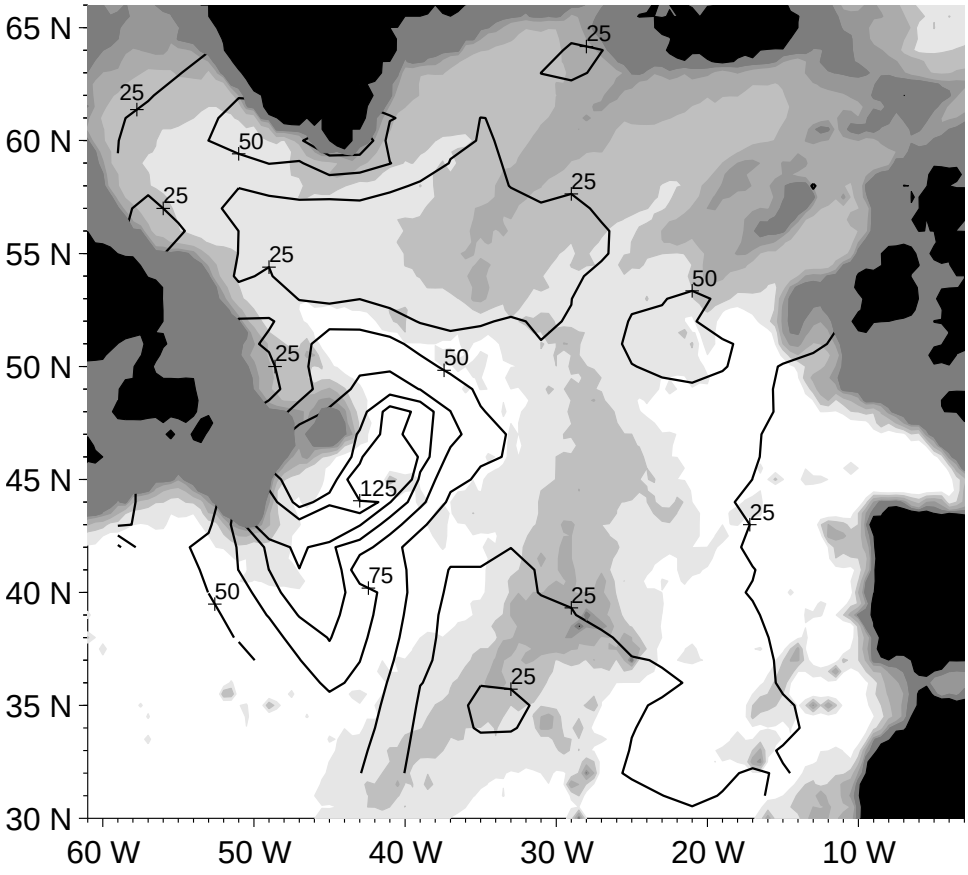

Figure 17: Eddy kinetic energy ($cm^2\ s^{-2}$) in the subpolar North Atlantic. EKE was estimated from departures of drift velocity data (adjusted to 700 m depth) from space-time averaged velocities that were locally smoothed (see text). Contour interval is 25 $cm^2\ s^{-2}$.

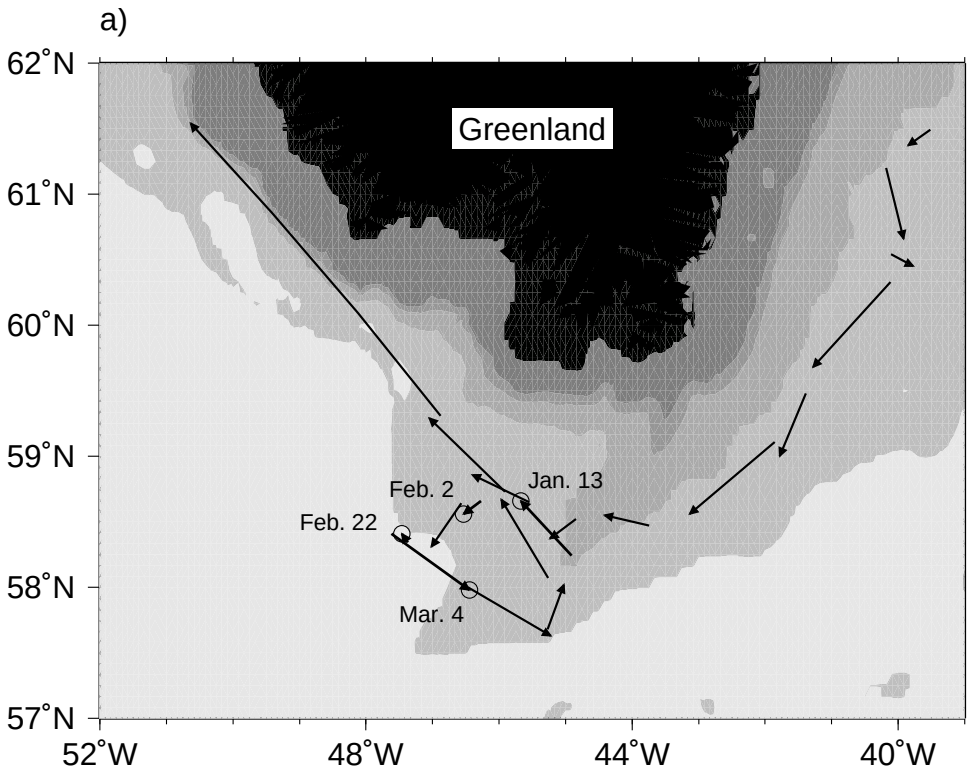
a)
62˚N
61˚N
60˚N
59˚N
58˚N
57˚N
52˚W
48˚W
44˚W
40˚W
Greenland
Jan. 13
Feb. 2
Feb. 22
Mar. 4

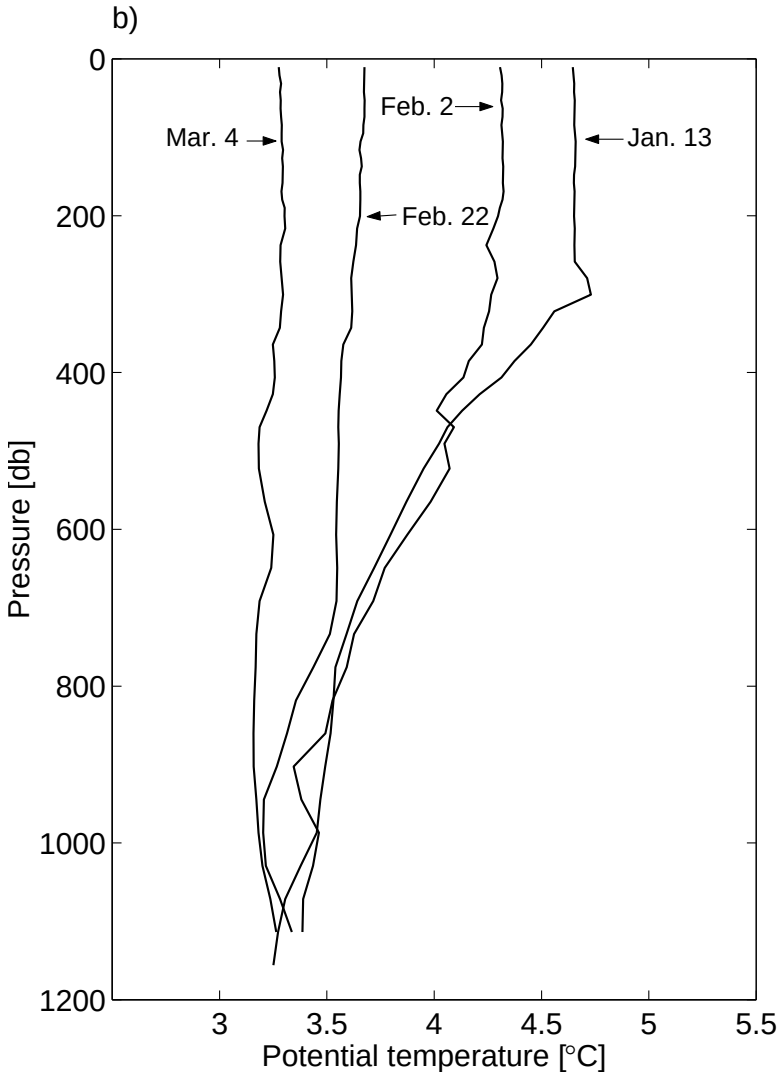

Figure 18: Active deep convection observed in the cyclonic recirculation southwest of the tip of Greenland from January–March, 2001. a) Nine-day float displacements at an average drift pressure of 640 db. Circles mark locations of temperature profiles. b) Profiles of potential temperature versus pressure measured while the float ascended to the surface at the end of its nine-day drift cycle. Progressive cooling and deepening of the mixed layer from roughly 300 m to 1100 m depth was observed over a period of weeks while the float drifted in the cyclonic gyre just offshore of the West Greenland Current.